NASA Technical Memorandum 86664

The Evaluation of a Number of Prototypes for the Free-Tip Rotor Constant-Moment Controller

Larry A. Young

February 1986

NASA

National Aeronautics and
Space Administration

The Evaluation of a Number of Prototypes for the Free-Tip Rotor Constant-Moment Controller

Larry A. Young, Ames Research Center, Moffett Field, California

February 1986

SUMMARY

This paper describes the development of several prototypes of a constant moment controller, a critical component of the free-tip rotor (FTR) concept. Also presented are the experimental results of a whirl test designed to select a final controller configuration to be included in a future wind-tunnel test of this innovative rotor system. A brief explanation of the FTR concept and its history are included. The paper documents the controller design constraints, each prototype's operating principle, the evaluation test, and the individual prototype test results. A recommended design is identified, along with the selection rationale.

LIST OF SYMBOLS

CF	centrifugal force of controller active mass, N
C_A	aerodynamic damping, N-m sec/rad
e	lag hinge offset, m
g	acceleration caused by gravity, 9.8 m/sec^2
I_C	controller polar moment of inertia, kg-m^2
I_e	equivalent polar moment of inertia of the controller and free tip, kg-m^2
I_{FT}	free-tip moment of inertia, kg-m^2
I_S	controller output shaft polar moment of inertia, kg-m^2
K	controller spring constant, N-m/rad
K_A	aerodynamic spring constant, N-m/rad
K_S	spring constant of the helical spring resisting the controller torque output, N-m/deg
l	torsion strap, active length, m
m	controller active mass, kg

R_m radial location of controller active mass, with respect to the axis of rotation, m

r torsion strap controller strap moment arm, m

r_c moment arm of the dual cam controller pin action, before cam angular displacement, m

r_{cg} moment arm of dual cam controller cam c.g, m

r_p mass-on-string controller pulley radius, m

r_s controller output shaft radius and moment arm length, m

T controller output torque, N-m

T_f moment caused by controller friction, N-m

T_0, T_1 special case torque expressions used in estimating controller torque variation with angular displacement, N-m

V velocity of the controller active mass, caused by controller output shaft angular velocity, m/sec

W weight of controller assembly, used for T_f calculation, N

x controller active mass radial translation caused by output shaft angular displacement, m

β controller out-of-plane angle, with reference plane perpendicular to axis of rotation, deg

δ change in controller torque output, %

μ controller friction coefficient, dimensionless

θ controller output shaft angular displacement, deg

θ_{PT} torsion strap pretwist, deg

$\Delta\theta$ torsion strap incremental displacement from pretwist angle, deg

ϕ angular displacement of controller cam, or torsion strap slope, deg

Ω test bed angular velocity, rad/sec

ω estimated parameter error

ω_d controller damped natural frequency, rad/sec

ζ controller in-plane angle, with the reference line perpendicular to the rotation axis and on a radial line from the hub centerline to the controller, deg

INTRODUCTION

Two major goals of helicopter research are rotor performance improvements and fixed-system vibration reductions. Present studies to improve performance are typically evolutionary in nature--a slow process of change in airfoil shapes, rotor twist, taper, spanwise camber distributions, tip shapes, and sweep angles. Similarly, hub vibration reduction studies seek to manipulate subtle parameters such as rotor mass distribution, and rotor and hub components' elastic stiffness and damping. The goal of an innovative concept, however, is to provide significant benefits by radically departing from conventional designs.

This paper is one of a series of publications describing the developmental history of the free-tip rotor (FTR) concept, references 1-5. The goals of the free-tip rotor are the reduction of fixed-system vibrations and increases in rotor performance while in forward flight, especially at high advance ratios. This paper deals with the development and testing of the constant moment controller, a critical component of the FTR concept.

The free-tip rotor is a conventional rotor except that the outermost portion of the blades have been modified to accommodate a free pitching tip (see figs. 1 and 2). Because of a moment balance about the tip's pitch axis, the tip passively changes its angle of attack in order to maintain nearly constant lift during the azimuthal sweep of the blade. The moment balance about the free tip is composed of the aerodynamic, inertial, and centrifugal moments on the tip and a moment that is applied by the controller.

Reference 1 indicates that a major portion of the total blade dynamic air loads are from the tip region (the outermost 10% of the blade). By torsionally decoupling the tip from the inner blade, and by allowing it to weathervane, the total dynamic loads should be reduced. However, two problems still remain. First, flapwise and chordwise loads will still be transmitted down the length of the blade. The FTR does, however, minimize these bending loads by forcing the tip to operate with a nearly constant lift. Second, in order to achieve complete torsional decoupling of the tip, the moment that is applied by the controller must be independent of the tip pitch angle, i.e., zero spring constant. This is difficult to accomplish. Thus, minimization of the spring constant is a major goal of FTR controller development.

The reasons for rotor performance improvements that result from the free-tip are not obvious. Reference 2 presents the original analytical feasibility study of the free-tip. Using a rotor performance program, comparisons were made between a conventional rotor and a free-tip rotor. The analysis was performed on a

3

three-bladed rotor, with a cruise speed of 140 knots, and a $C_T/\sigma = 0.07$. The results indicated a 10% reduction in rotor C_P/σ because of the free tip. Reference 2 cites the more uniform lift distribution of the blade about the azimuth as being the mechanism for the FTR performance gains.

The developmental history of the free-tip rotor has been a long one. The predecessor of the FTR is the constant-lift rotor, reference 3. After the early analytical effort of reference 2, a program was initiated to develop a prototype FTR controller and to test the resulting mechanism by performing a wind tunnel test. The results are documented in references 4 and 5. From this study a prototype was developed that met the concept requirements. As can be seen from figure 3, this early controller design's mechanics were simple. The principle of operation of the controller was the same as that of a power screw: an axial force acting on a helical surface imparts not only a normal force to the surface but also a torque. In the case of the free-tip controller the axial force was the tip's centrifugal force and the resulting torque was the controller moment. However, the unavoidable surface contact force caused significant problems during the wind tunnel test. The results of this first forward-flight wind tunnel test showed that the FTR incorporating this helical angle controller had little tip pitch response as the blade rotated to different azimuthal positions. Analysis of the test results and the mechanism components supported the conclusion that the high stresses resulting from the contact force led to elastic deflections which were sufficient to cause partial immobilization of the follower pin and, consequently, the tip. Since the restriction of tip pitching motion is detrimental to the free-tip concept, and as the contact force could not be reduced without significantly reducing the desired torque output, the helical guide/follower prototype was found to be impractical. Reducing controller component elastic deformations by using a stiffer material was considered, but a material could not be found that had a satisfactory yield strength.

In order to experimentally evaluate the free-tip concept, it was necessary to have a viable device that provided the required torque output and that allowed the tip to pitch with minimum restriction. Therefore, because of the helical guide/follower prototype controller's failure, a new controller design was needed.

Despite the inability to meet the primary goal of the first wind tunnel test, valuable lessons were learned from the experience. The first was a tangible demonstration of the difficulty of designing mechanisms to survive the high centripetal accelerations and loads of helicopter blade tips. Another was the need for a new approach to the controller problem. Wind tunnel tests are too expensive and time-consuming to develop or to evaluate a large number of controller prototypes. To be able to refine the new generation of proposed controllers, an intermediate development stage using an inexpensive means to apply centrifugal loading to the controllers was necessary.

4

DESIGN APPROACH

A comprehensive controller development program, which is the subject of this paper, was initiated subject to one precept: to not enter into a wind tunnel test again until a workable FTR controller had been demonstrated. Improvements in the prototype design approach were made. The original approach eliminated competing concepts early in the design process, leaving only a single candidate to undergo complete development. This design was not adequately tested prior to tunnel entry. The first prototype was incapable of providing the required performance. This was discovered late in the program. Therefore, four guidelines were adopted as the basic philosophy for this new controller development program to increase the likelihood of developing a successful free-tip controller.

The four prototype development guidelines were:

1. Maximize the number of controller concepts considered in the preliminary stages of the development program. (The key to this objective is to avoid early assessment of implementation feasibility.) A greater diversity and number of controller concepts were likely to improve the chances for identifying a successful prototype.

2. Maximize the use of common components for noncritical features and subsystems of the prototypes. The advantage of this policy is that it minimizes the time required for the design, fabrication, and testing of a controller by reducing the number of unique components. The quality and number of prototypes could then be increased through compatibility.

3. Maximize the number of controller prototypes to reach the testing phase of the development program, by emphasizing diversity in prototype operating principles. By meeting this objective, the likelihood of eliminating all prototype candidates during the feasibility testing is reduced.

4. Subject each controller design to the same constraints as the wind tunnel model configuration. By doing this, two things can be accomplished: the redesign effort that is necessary to arrive at a free-tip rotor which is compatible with the controller is minimized, and the likelihood of accepting an infeasible design is reduced.

Aside from the above guidelines, the first step in any design process is the definition of the technical problem. In this case, the controller prototypes were subject to two types of constraints: conceptual and package constraints. Conceptual constraints are those mandatory design requirements which the prototype must satisfy. Package specifications are those constraints that must be satisfied in order to have a design that can be physically realized for the particular application considered. A brief example is "constant moment," which is a conceptual constraint, whereas controller dimensions are package constraints. The following items comprise the list of the applicable conceptual FTR controller constraints.

5

1. The FTR controller must be capable of applying a moment to a rotor-blade tip. The moment should be preflight-adjustable from 0 to 6.78 N-m. The moment upper limit was based on an estimated pitch-axis offset and maximum lift for the tip shapes that were considered for the FTR concept.

2. The controller should have a zero spring constant; therefore, within specified tip pitch limits the torque output of the controller should not vary significantly. Because of friction and other factors, this is not attainable. Therefore, for this design exercise and the subsequent prototype evaluation testing, the following realistic requirements were established: for the allowable pitch range of ±10° the controller torque was not to vary by more than 10% of the average value.

3. The controller mechanism must be capable of operating under centrifugal and aerodynamic loading equivalent to that which it would have to endure during a wind tunnel test at full-scale rotor tip speeds.

4. Limit the controller shaft/tip bending alternating stresses so as to have a fatigue life of at least 100 hr, under maximum centrifugal loading. Therefore, controller candidates must be subjected to cyclic loading in order to determine fatigue life as a part of the prototype testing.

The package constraints are as follows:

1. The controller must fit within the steel D spars of a 5.1-m diam model rotor having a V23010-1.58 airfoil contour and a solidity of 0.085. Therefore, the maximum thickness of the controller was limited to 0.015 m, and its outer contour was determined by the D spar's interior dimensions.

2. The controller had to accommodate a 10% 0.254-m span tip. For acceptable tip dynamic characteristics, the tip was required to be mass-balanced about the pitch axis. This further increased the centrifugal loading to which the controller had to react. The loads were estimated by doubling the mass of a previously tested 5% tip (ref. 4).

3. The method of attaching the controller to the rotor blade must ensure a high structural factor of safety (greater than 2, based on yield strength), and allow the controller to be detachable (without damaging the blade or the controller).

4. The design should minimize the necessity of removing the controller from the blade to make minor mechanical adjustments. For example, it must be possible to be able to vary the torque output without removing the controller.

Using the above constraints, four controller prototypes were designed. These controllers were designated as: dual cam controller (DCC); mass-on-the-string controller, pulley version (MOS); mass-on-the string controller, cam version (MOS2); and torsion strap controller (TSC).

CONTROLLER DESIGNS

This section will concentrate on describing the actual mechanisms that were tested, including their operating principles and their design details. Four controller prototypes were considered in the testing phase. Figures 4 through 7 illustrate the final designs. The next several paragraphs will be devoted to descriptions of each individual prototype.

The Dual-Cam Controller

The dual-cam controller is based on the following principles of operation: first, the centrifugal loading on the mechanism provides the output torque; second, the conversion of force to torque is accomplished through a spatial linkage system. Refer to figure 4(a) for the DCC assembly drawing. For simplicity, subsequent discussion will consider just one of the controller's two cams. In figure 4(b), the centrifugal force on the cam can be seen to be operating at its c.g. in the radial direction. The force acting on the pivoted cam imparts a moment; since the cam is slotted and has a pin riding in it, it applies a force through cam action to that pin. When this force is applied to the pin which is attached to the output shaft, the required DCC control moment is produced. The length of the DCC spatial mechanism's individual linkage arms were proportioned so as to provide the required shaft moment range that was demanded by the design constraints. There are four parameters that could be varied in order to vary torque output: the three linkage lengths and the mass of the cams. The main constraint on these parameters was the space requirements of the design: the mass and the linkages had to fit within the package envelope of the design. The redundancy of the dual-cam approach, as compared to a single cam design, was required to reduce the high-contact (Hertz) stresses that are generated on the pin and on the cam's slot. Additionally, it was found that because the cam's c.g. was below its centerline, a twisting moment was applied to the single cam; this caused increased friction and scarring at the cam/shaft interface. Use of a dual-cam configuration minimized this problem.

Figure 4(b) illustrates the DCC linkage motion that occurs when the controller responds to free-tip pitching. As the tip pitches, the controller's shaft rotates. The shaft rotation, in turn, will drive the pin against the slotted cam surface causing the cam to rotate about an axis perpendicular to the shaft axis. Additionally, as the cam rotates, the c.g. of the cam translates with respect to the radial axis of the blade, or in this case, the rotating test bed. Therefore, the kinematics of the dual-cam controller demand that small changes in the control torque must occur as the free-tip pitches. Another consequence of the cam's rotation is that it enforces a specified pitch range limit: at the limit, the cam rotates into a portion of the controller housing.

Mass-on-String Controller, Pulley Version

Figure 5 shows the mass-on-string controller, pulley version (MOS). Figure 5(a) is an assembly drawing of the controller; figure 5(b) is its free-body diagram and kinematic sketch. The MOS controller, like the DCC, also derives its output torque from centrifugal force. The critical problem is the mechanical conversion of force to torque. In this particular design a cable and pulley system is the solution. A mass attached to one end of the cable provides the centrifugal loading; the cable wrapped around the pulley and the output shaft allows the cable tension to be applied to the shaft's outer radius resulting in the desired control moment.

Referring to figure 5(b), the MOS controller torque output is the mass centrifugal load multiplied by the shaft moment arm, r_s. Therefore, the parameters which govern the MOS control moment are the rotating frame rpm, the active-mass c.g. location with respect to the rotating frame axis (R_m), the output shaft radius (r_s), and the active-mass magnitude (m). Of these four parameters, only m can be varied significantly without violating design constraints or structural limits. Package size limits are not violated by moderate mass increases if the length of the mass is increased.

The major advantages of the MOS approach are its mechanical simplicity and the increased capacity for torque output as compared to the DCC design. Its chief disadvantage is the poor durability of the kevlar chord when the chord comes in contact with the shaft's small turn radii. Another minor disadvantage of the MOS design is a nonzero spring constant, which is in this case due to a change in the centrifugal load of the active mass resulting from the mass translation along a radial line necessitated by output shaft pitching. However, the MOS spring constant is well within design constraints as will be demonstrated in the analytical results section. Mass translation as a result of output shaft angular displacement can be clearly seen in figure 5(b). As the output shaft displaces an angle θ, the cable unwinds a set length which is equal to the fraction of the circumference of the output shaft that a point located on the nominal diameter would rotate. The mass c.g. translates radially by that amount.

Mass-on-String Controller, Cam Version

Figure 6 shows the mass-on-string controller, cam version (MOS2). The operative principle of this prototype is the same as the MOS controller. There is only one hardware difference between the two controllers: instead of a pulley, there is a cam to change the cable translation direction. All other controller components are compatible. The only significant difference that can be seen between the two controllers in figure 6 (the force free-body diagram) is that the cam offers a mechanical advantage over the pulley in that additional leverage can be applied; therefore, with the MOS2 design, the mass centrifugal load can be reduced and an equivalent torque output can still be obtained. An expression for the cam mechanical advantage is

8

$$\text{mechanical advantage} = \frac{r_{cg}}{r_c}$$

In terms of kinematics, the cam version prototype is similar to the MOS design. However, a significant difference between the two designs is that for a given θ, the cam rotation ϕ causes a greater translation of the active mass than the pulley prototype does, because of the mechanical advantage of the cam design.

Torsion Strap Controller

Figure 7(a) is the assembly drawing of the torsion strap controller (TSC); figure 7(b) is a free-body diagram of one of the controller's two fine wire straps. The mechanics of this controller are very simple. The TSC derives its torque output from two sources: the majority of the torque comes from tensile loading of twisted wire straps, whereas the remainder is due to the elastic properties of the wires and elastomeric filler when under torsion. The strap tensile loading is due to the centripetal acceleration on the mass of the output shaft and on the hardware attached to it (including the tip mass in the FTR model).

Figure 7(b) shows the operation of the TSC. The torque output of the controller is a function of the strap radius and the centrifugal load of the controller active mass. The active mass is the combined mass of the output shaft, torsion straps, and, in the case of the whirl test, a spring assembly. Referring to the figure insets of an incremental strap segment, this torque-producing force component is found to be dependent not only on the CF, but also on ϕ, defined for the TSC as the strap twist. The strap twist is a function of the strap length, strap radius, and the absolute angular displacement of the output shaft, $\theta_{PT} + \Delta\theta$; the TSC strap can have a pretwist, θ_{PT}, as well as a $\Delta\theta$ displacement under centrifugal loading. Because of design constraints (size limitations on the strap radius and length, and structural limitations on the active mass centrifugal load) the TSC torque output was varied during the whirl test by varying the strap pretwist angle, θ_{PT}.

Common Controller Components

One of the objectives of this development program was the use of common controller features so as to simplify the design, fabrication, and testing of the prototypes. Several features of controller component compatibility are discussed below.

The dual-cam controller (refer to fig. 4(a)) incorporates a feature common to three of the controller designs: the method for axially restraining the shaft and tip. The cable assembly allows as much flexibility for shaft rotation as possible so as to minimize the spring constant of the controller. The cable assembly is fastened to the inboard end of the controller output shaft. With the elimination of thrust bearings as component candidates for this task, because of size and load constraints, a long thin cable was considered to be the next best solution.

The DCC, MOS, and MOS2 controllers utilized the same basic housing and output shaft using only minor modifications. The next common feature for most of the controllers designed is the general features of the torque output/tip attachment shaft. Finally, in all controllers that were tested during the whirl test, the same general provision was made for connecting the controllers to a mechanical spring so as to simulate an aerodynamic spring and also to provide a means for resisting the controller's torque output.

WHIRL TEST APPARATUS

Whirl Rig

Figure 8 is a photograph of the whirl rig. The rig was a centrifuge designed for the prototype evaluation test. The purpose of this rig was to provide a rotating test bed that could impart the same centrifugal loads that the controllers would have to undergo during a rotor wind-tunnel test. The rig was 1.68 m high and had a diameter of 2.0 m. The rig was powered by a 93.2 kw electric motor; the motor was housed in an aluminum block, and clamped into place by a collar. The electric motor drove the centrifuge's main shaft through a v-belt and a spindle. The whirl rig main shaft was hollow so as to provide a convenient conduit for the instrumentation cables that ran up the rotating test bed.

The whirl rig test bed was an aluminum plate upon which the experimental apparatus was mounted. Figure 9 shows the test bed with the equipment assemblies mounted on it. The rotating test bed was a rectangular plate with rounded ends. There were three major assemblies on the plate during the evaluation testing of the controller prototypes: the controller, the counterweight, and the exciter. The exciter was a critical hardware component. The exciter provided the means with which to pitch the controller output shaft during the whirl test, so as to observe the effect of θ on torque. Additionally, the exciter displaced the controller output shaft from its steady-state position so that the transient response of each design could be measured.

Exciter

Figure 10 is an assembly drawing of the exciter. Looking inboard, the exciter consists of a remote-controlled cam and trip-lever assembly for perturbing each controller prototype from its equilibrium point.

The apparatus that was used to perturb the controller static moment equilibrium is composed of two major components: a torsion spring assembly and the exciter. A helical torsion spring was used to resist the torque output of the controllers. The helical torsion spring, with mandrel, was attached at opposite ends to both the output shaft and the whirl rig test bed. In addition to making a steady state moment balance possible, the spring assembly mandrel was designed so as to also act as the trip lever for the exciter cam.

The exciter cam was driven by an aluminum shaft which was connected to a constant velocity electric motor that was mounted close to the rotating test bed axis (see fig. 9). Electric current was supplied through the whirl rig slip ring. The cam was a small diameter dowel that was mounted on a disk face. By rotating either clockwise or counterclockwise, the extended dowel would engage the trip lever and displace the controller/torsion spring from the equilibrium point (see fig. 10). As the cam continued to rotate, the trip lever would slip off the dowel. The response of the controller/torsion spring dynamic system to this perturbation was measured.

WHIRL TEST PROCEDURES

The following is a general outline of the whirl test procedures:

1. Set whirl rig rpm to specified value.

2. Record transducer values indicating controller output shaft angular deflections. Readings made by means of a multichannel voltmeter.

3. Determine the magnitude and relative location of the maximum Hall effect voltage by disturbing the shaft from its equilibrium point through clockwise and counterclockwise exciter rotations. The shaft angle transducer calibration is thereby completed.

4. Produce controller dynamic responses to exciter clockwise and counterclockwise perturbations. Record the response on analog tape and oscillograph paper. Log the new equilibrium points.

5. Return to the first step until maximum rpm has been attained.

During the test there were four transducers that provided information about controller performance under centrifugal loading: the Hall effect device, foil and semiconductor strain gages, and a resistance (wiper) pot. Not all of these transducers were applicable to all of the controllers, nor were all of the transducers working nominally all the time. The first transducer to be discussed is the Hall effect.

The Hall effect (ref. 6) is an electrical circuit whose voltage output is sensitive to magnetic flux. The Hall effect transducer was a small semiconductor device based on this principle. In this test the transducer was used to measure θ; it was the primary data measurement of the experiment. Since magnetic flux varies with distance from the source, by locating the transducer on the controller housing with a permanent magnet attached to the exciter-cam follower, a measurement of the controller's shaft rotation can be made by the decrease in the magnetic flux as the magnet rotates away from the transducer (refer to fig. 11). The pitch angle, given the spring constant of the torsional spring, was used to calculate each controller's moment output. Both the voltage vs pitch and the pitch vs torque relationships for the Hall effect transducer were developed through calibration.

The combined procedure for the Hall effect transducer calibration and for obtaining the spring constant of the output shaft spring assembly was as follows:

1. A pulley/cable assembly was mated to the end of the output shaft.

2. Knowing the radius of the pulley, a torque was applied to the shaft by adding known weights to the end of the cable.

3. The applied torque deflected the torsion spring to an angle.

4. Both the Hall-effect voltage and the trip-lever scale measurements were recorded.

5. The spring constant was determined by a linear fit of the spring deflection and the applied moment data set.

A wiper pot transducer was installed as an alternative to the Hall-effect device, and the same type of calibrations and calculations are applicable. Unfortunately, the wiper pot was plagued throughout the test with failures: with the whirl rig set at zero rpm, the pot gave linear, repeatable calibrations; with the whirl rig rotating, the wiper pot signal degenerated into noise.

The foil and semiconductor strain gages both rely upon the same basic principle to provide an estimate of the controller's torque. The foil and semiconductor strain gages were arranged about the circumference of the output shaft, as shown in figure 12. The gages were oriented and bridged to measure only the strain caused by torsion and not to react to tensile or bending loads. The calibration hardware used was the same as that used in the torque vs pitch measurements. The strain gage voltages were measured to obtain a torque vs voltage curve. Therefore, at each test point, the strain gage voltages were measured and compared to the calibration curve, and the controller torque output was estimated. When compared to results obtained by the Hall-effect technique, the strain gages worked satisfactorily for one of the two controller prototypes, but performed poorly on the second. Further investigation revealed that the second pair of strain gages were improperly oriented on the shaft so that bending and tensile loads were also being measured.

Therefore, the Hall-effect device was the only reliable transducer that was used during this test, and it was the primary source of experimental results. However, potential errors in the estimates of the controller torque output, beyond those of instrumentation accuracy, are possible.

Friction is detrimental to controller performance. Friction could possibly either restrict shaft rotation or reduce torque output. Steps were taken to estimate the resisting moment caused by the friction of the controller and spring assembly. This included conducting an rpm sweep and perturbing the controller from its equilibrium position by using clockwise and counterclockwise exciter rotations. By perturbing the shaft from its equilibrium position, motion restricted by friction should be apparent from the dynamic response. Additionally, differences in equilibrium points could be in part due to friction.

Another potential torque output estimate error source is the effect of cable stretch on the experimental measurements. As stated previously, the Hall-effect transducer output voltage is dependent upon not only angular displacements, but it is also a function of the total distance from the magnetic source. The cable attached to the shaft of three of the four controllers is subjected to the centrifugal load of the whole free-tip assembly. As the cable stretches under centrifugal load, the output of the Hall-effect transducer changes, even if no pitch motion occurs. In order to minimize the errors that are due to cable stretch, the maximum Hall-effect voltage and its angular location relative to the equilibrium point was noted at each test point. By assuming that the maximum voltage occurs at a constant pitch angle, the Hall-effect calibration curve can be scaled for each test point. In this manner the θ measurements were corrected for cable stretch.

The mechanical torsion spring has two attachment points which allow it to resist the torque that is produced by the controller. One attachment point is on the controller housing and the other is connected to the output shaft. The spring terminations were loosely attached. The consequence of this loose attachment is a potential inaccuracy in the pitch equilibrium point, thus affecting the torque calculation. Alternating the direction of the exciter perturbations did reveal a consistent upper and lower limit to the pitch angle measurements at all rpms. A portion of this experimental uncertainty of the torque estimates must be due to the spring play; some of the remaining contributions to this data scatter are friction and instrumentation accuracy.

ANALYTICAL RESULTS

The free-tip motion can be modeled by the expression

$$I_e \ddot{\theta} + C_A \dot{\theta} + (K_A + K)\theta + T_f = M(t)$$

where θ, I_e, C_A, K_A, K, and T_f are the pitch angle, system inertia, aerodynamic damping and spring, controller spring, and the torque friction component, respectively. $M(t)$ is a summation of external moments as a function of time (azimuth). These moments include: the controller output torque, centrifugal-tip moment, and inertial moments. Further, the summation of these moments determines the free-tip's steady-state pitch displacement.

Analytical expressions for I_e, K, T_f, and the controller output torque for each of the prototypes are summarized below. The purpose of this work is the selection of viable controller prototypes that are suitable for wind-tunnel testing of the free-tip rotor concept.

Two analytical models are derived for controller torque output. One is a simplistic model that ignores the effect of controller shaft pitching deflections on the control moment. The other model takes into account the angular displacement effects. The two models are identified respectively as the theta-independent and

13

the theta-dependent torque output models. Appendix A contains the torque output model derivations for each of the controllers.

Uncertainty estimates were made of the controller torque output model predictions by employing the analysis method presented in reference 7. Appendix B presents the uncertainty analysis as applied to the free-tip controller prediction models. Tables 1-3 contain the independent parameter accuracies that were used in the uncertainty calculations.

Besides providing a steady-state control moment, the free-tip controller output shaft is subjected to high-frequency pitching oscillations. The dynamic behavior of each controller is defined by its equivalent inertia, spring constant, and damping coefficient. Appendix C derives equivalent inertia expressions for the controllers based upon a kinetic energy approach. Appendix D derives controller spring constants based upon the torque output models derived in appendix A. Appendix E derives coulomb damping expressions, T_f, for each controller.

The following equations summarize the results of the above noted analytical derivations.

Dual Cam Controller

<u>Theta-independent torque output model</u> (fig. 4(b)):

$$T = \frac{1}{r_c} m\Omega^2 R_m r_{cg} r_s \tag{1}$$

<u>Theta-dependent torque output model</u> (fig. 4(b)):

$$T = \frac{1}{r_c} m\Omega^2 (R_m + x) r_{cg} r_s \cos^3 \phi \tag{2a}$$

where

$$x = r_{cg} \sin \phi \tag{2b}$$

$$\phi = \tan^{-1} \left(\frac{r_s}{r_c} \tan \theta \right) \tag{2c}$$

Note that for the experimental configuration

$$\theta = \theta_0 - T/K_s \tag{2d}$$

14

Equivalent inertia (ref. 8)

$$I_e = I_{FT} + I_s + I_c \left(\frac{r_s}{r_c} \right)^2$$
(3)

Spring constant

$$K_{dcc} = m\Omega^2 \left(\frac{r_{cg} r_s}{r_c} \right)^2$$
(4)

Damping coefficient (figs. 13 and 14(a))

$$T_f = T_{f(shaft)} + T_{f(dcc)}$$
(5)

where

$$T_{f(shaft)} = \mu r_s \sqrt{(W \cos \beta)^2 + (CF \sin \beta)^2 + (CF \sin \zeta)^2}$$

$$T_{f(dcc)} = \mu \frac{r_{cg} r_s}{r_c} N_{dcc}$$

and

$$N_{dcc} = W_{dcc} \cos \beta + CF_{dcc} \sin \beta$$

Mass-on-String, Pulley Version (fig. 5(b))

Theta-independent torque output model:

$$T = m\Omega^2 R_m r_s$$
(6)

Theta-dependent torque output model:

$$T = m\Omega^2 [R_m + \theta r_s] r_s$$
(7a)

or for the whirl test

$$T = \frac{m\Omega^2 R_m r}{[1 - (r_s^2/K_S)m\Omega^2]}$$
(7b)

Equivalent inertia

$$I_e = I_{FT} + I_s + I_p \left(\frac{r_s}{r_p}\right)^2 + mr_s^2 \qquad (8)$$

Spring constant

$$K_{mos} = [m(\Omega r_s)^2] \qquad (9)$$

Damping coefficient (fig. 14(b))

$$T_f = T_{f(shaft)} + T_{f(mos)} \qquad (10)$$

$$T_{f(mos)} = \mu r_s N_{mos}$$

where

$$N_{mos} = \sqrt{(W_{mos} \cos \beta)^2 + (CF_{mos} \sin \beta)^2 + (CF_{mos} \sin \zeta)^2}$$

Torsion Strap Controller

Theta-independent torque output model (fig. 7(b)):

$$\theta = \theta_{PT}$$

applied to equation (11).

Theta-dependent torque output model (fig. 7(b)):

$$\theta = \theta_{PT} + \Delta\theta$$

applied to equation (11).

$$\theta = \theta_{PT} - T/K_S$$

is a special case for whirl test predictions.

$$T = rm\Omega^2 R_m \tan \phi \qquad (11a)$$

$$\phi = \tan^{-1}\left(\frac{\theta r}{l}\right) \qquad (11b)$$

16

Equivalent inertia

$$I_e = I_{FT} + I_s \tag{12}$$

Spring constant

$$K_{tsc} = m(\Omega r)^2 \, \frac{R_m}{l} \tag{13}$$

Damping coefficient

$$T_f = T_{f(shaft)} \tag{14}$$

where $T_{f(shaft)}$ is as previously defined.

EXPERIMENTAL RESULTS

The Dual Cam Controller

Figures 15 and 16(a) are examples of the calibration curves employed in the controller torque output data reduction. A linear curve fit was made from the strain gage calibration data and used to calculate control moments based upon test point gage readings. Because of the nonlinearity of the Hall-effect calibration curve, pitch estimates and, therefore, torque values were interpolated from tabulated data.

The pitch angle is nonunique with respect to the Hall-effect voltage output as shown in the figure 16(a) calibration curve. A voltage reading has two possible θ interpretations. An additional piece of information is required to select the correct pitch angle. The maximum voltage peak was, therefore, located for each test point by the exciter cam rotation of the controller trip lever and magnet. The relative location of the peak voltage with respect to the test point measurement (clockwise or counterclockwise) defined which portion of the calibration curve the test point θ was to be read from. The output shaft angular deflections in conjunction with the resisting spring constant (fig. 16(b)) are used to calculate the control moment.

Figure 17 presents the whirl test results in a plot of the DCC prototype's torque output as a function of rpm. The DCC experimental data shown in figure 17 was obtained from three transducers. There is good agreement between the Hall effect and the strain gage estimated torque output results. This correlation establishes the validity of the Hall-effect results, especially important since it was the only transducer operative for the remainder of the test.

Also plotted in figure 17 are the predicted results of equation (2). The model is in good agreement with the experimental data in the rpm range roughly from $0 <$ rpm < 700, or approximately 30% of an anticipated full-scale/free-tip rotor tip centripetal acceleration. For rpm greater than 700 there is an increasingly

17

significant overprediction of the torque output. The experimental data scatter and the large uncertainty of the torque output predictions make it difficult to judge the correlation between the analytical and experimental results. However, it is clear that there is some phenomenom that is not accounted for in equation (2). One possible explanation for this poor correlation is that of friction resisting the torque output.

Although it is apparent that the DCC analytical model requires refinement, that is not the primary concern of the whirl test. The chief objective of this test was the evaluation of the controller prototypes. Figure 17 suggests that the DCC active mass must be approximately tripled in order to produce the required maximum torque output. However, the DCC design has insufficient space available to accommodate this large mass increase which is subject to the restrictive controller dimensional tolerances (see fig. 4(a)). Additionally, the pin and cam slot contact stresses would substantially increase with the added mass. Therefore, the DCC concept seems unable to meet the design specifications. It should be noted that there is one more problem with the DCC: the prototype is difficult to assemble and to maintain.

The Mass-on-String Controller, Pulley Version

Figure 18 shows experimental data based on the Hall-effect transducer when compared with the predicted results from equation (7). There is again significant disagreements between the experimental data and the theory. However, when compared to the DCC prediction results, the MOS predictions are much better. Correlation is again difficult because the analytical prediction uncertainties are substantial. An important disagreement between the two sets of data is at the lower rpm range. There the experimental torque values are high and the overall empirical trend is biased. Unfortunately, a lack of data in this rpm range prevents a better comparison. The most important aspect of the MOS evaluation was that although the controller was not functioning as was predicted, the experimental data still showed the amount of additional mass that was necessary to produce the design's specified maximum torque output. The maximum MOS torque output was 27% of the 6.78 N-m design goal. This result indicates that a 3 to 1 mass increase is necessary. The space available and the structural limits of the MOS design can accommodate the additional mass. Thus, from this standpoint, the MOS prototype remains a viable concept for the free-tip controller.

However, the uncoated Kevlar fibers, by which the mass centrifugal force was applied to the output shaft, were showing signs of wear. The fiber bundles wrapped about the output shaft's small radius were spreading thin and were separating. There were no signs of fiber breakage, but it was clear that it was only a matter of time before failure would have occurred. It is therefore necessary to find alternative materials and antiabrasion coatings before employing this concept in a wind-tunnel test.

The Mass-on-String Controller, Cam Version

This concept was proposed as a means to retain the basic conceptual character-
istics of the MOS prototype, while at the same time reducing fiber abrasion: the
fiber abrasion would be reduced because the fibers would no longer be rubbing along
a pulley, but would instead be bonded directly to the cam.

Fabrication problems and also tight dimensional tolerances prohibited the
testing of the MOS2 concept. A small amount of cord slack resulted from the fabri-
cation so that the cam could completely rotate within its package limits and yet the
cord about the output shaft would not have a significant tensile load applied to
it. Subsequent modification efforts were unsuccessful and so data was not acquired
for this prototype.

The Torsion Strap Controller

It was demonstrated (eq. (11)) that the torsion strap controller's torque
output was a function of two parameters which were varied during the whirl test:
the controller tensile loading and the strap pretwist angle. The controller cen-
trifugal force (CF)/tensile load was varied by changing the whirl-rig rpm. Fig-
ures 19 through 22 are plots of the experimental and predicted TSC torque as a
function of both these parameters. Similar to the other controller designs, the TSC
torque output predictions have large uncertainties, given the accuracy of the input
parameters used in the model. Table 3 contains the value and accuracies of the TSC
parameters. The table values are based upon measurements of the TSC design that was
tested during the whirl test. In addition to the prediction uncertainty, there is
significant data scatter in the torque measurements. This data scatter is due to a
number of factors including instrumentation sensitivity, poor spring assembly
attachment to the controller output shaft, and friction. For these reasons the TSC
(and the other controllers) theoretical and experimental comparisons are only quali-
tative. However, the functional nature of both trends demonstrate similarities.

To determine whether or not the functional form of the analytical TSC model
(i.e., parabolic with respect to rpm and linear for θ) is representative of the
experimental data, a regression analysis was performed. A semiempirical form of a
linearized equation (11) (with respect to θ) was proposed.

$$T = C\theta\Omega^2 \qquad\qquad (15)$$

where C is a constant derived by least square regression of one of the four TSC
experimental data sets. The constant C in the semiempirical model replaces the
strap geometry parameters of the analytical model. Both the analytical and semi-
empirical model are to be considered representative of the experimental data if the
value of C derived by regression analysis is approximately the value analytically
specified, resulting in prediction improvements of the other data sets.

For the TSC whirl test comparison, the resisting helical spring torque con-
straint must be applied, i.e.,

$$\theta = \theta_{PT} - T/K_S$$

Therefore, for the regression analysis of the whirl test data the semiempirical model, taking into account the spring constraint, must be expressed as

$$T = \frac{C\theta_{PT}\Omega^2}{[1 + (C\Omega^2/K)]} \tag{16}$$

if the controller output shaft pitch angles are expressed in terms of the initial strap pretwist angle, θ_{PT}, and the resisting spring deflection.

Alternatively, equation (15) can be used for the regression analysis if the experimental θ measurements are included in the calculation in addition to the torque and rpm values.

For the following analysis, equation (15) was used to define the least-square regression error function. After deriving the constant C, equation (16) was used to calculate the resulting semiempirical predictions.

Therefore, the error function can be defined as

$$E = \sum_{i=0}^{N} [C\theta_i\Omega_i^2 - T_i]^2$$

where θ_i, Ω_i, and T_i are the regression analysis input parameters.

By minimizing the error function the coefficient, C, is determined

$$\frac{\partial E}{\partial C} = 0$$

thus

$$C = \frac{\displaystyle\sum_{i=0}^{N} T_i\theta_i\Omega_i^2}{\displaystyle\sum_{i=0}^{N} (\theta_i\Omega_i^2)^2} \tag{17}$$

Using the $\theta_{PT} = 67°$ data set for the least-square fit, the above equation resulted in an empirical coefficient, C, which was only 8% different from the analytically derived coefficient. However, the semiempirical predictions of equation (16) demonstrate a large correlation improvement with the remaining θ_{PT} data sets, as shown in figures 23 through 25. The reason for the 8% coefficient correction resulting in 20-30% prediction improvement is that the torque dependence on C in equation (16) is nonlinear. Additionally, the spring deflection (thus, a

portion of the nonlinear C dependence) was accounted for by using experimental θ_i values in the regression analysis, equation (15).

Because there is only a small difference between the analytical and experimental derivation of C, and because of the satisfactory correlation of the semiempirical model with experimental data, the functional form of both the analytical and semiempirical models are correct. To obtain reasonable future TSC torque output predictions, two approaches can be taken.

First, the analytical model may be used if extreme accuracy in specifying the input parameters is achieved. This task is difficult because of the small size and construction of the TSC. It is further complicated by small but significant geometry changes that are caused by the application of tensile loads on the straps while under CF.

Second, the semiempirical model can be used if a TSC pull test calibration is conducted where the straps can be pretwisted, tensile loads can be applied, and the straps' resulting torque output can be measured. By using the pull test data set, the above demonstrated regression analysis can be performed. As a result, this analysis can be used as an accurate semiempirical TSC model.

Unlike the other controller prototypes, space limitations do not necessarily limit the TSC torque output; the maximum pitch pretwist angle is not limited by the space requirements. Increasing the controller's active mass is an alternative approach to increasing torque output, but this method is constrained by package limits. In this particular test, torque was restricted by a pretwist structural limit. However, it appears likely that the TSC design is capable of meeting the design constraint of the controller's maximum torque output.

Dynamic Characteristics

The experimental apparatus provided information about each prototype's dynamic behavior. Oscillograph traces of the Hall-effect voltage as the prototypes were perturbed revealed two things: the controller-spring system had responses measured in the hundredths of a second and all but the TSC responses were overdamped. These factors made analysis impossible for all prototypes except for the TSC, and determination of the dynamic coefficients of that controller was extremely difficult. Two methods were employed to experimentally estimate the TSC spring constant and damping coefficient.

The first method determined the T_f of the total torsion spring-controller system from the static deflection data. In acquiring dynamic traces it was observed that the TSC steady-state equilibrium output torque was dependent on the direction of the initial deflection. This observation agrees with the dynamic behavior of a mechanical system which has large coulomb damping. If it is assumed that the differences in torque output were due completely to static friction, then an estimate of T_f contribution could be made. The first step in this analysis is to calculate the mean torque output per test point. The second step is the calculation of the

test-point torque output standard deviation. Since differences in torque output for alternating exciter perturbations were assumed for a worst-case analysis to be totally due to static friction, the standard deviation estimate is also a measure of T_f (the torque component that is due to friction). The estimates for T_f when the above statistical calculations are performed are shown in table 4.

The average T_f from table 4 was approximately 0.0226 N-m. Equation (14) estimates the T_f to be 0.0113 N-m, for a friction coefficient of 0.5 (a valid number for the brass on steel controller bearing surface), assuming that the out-of-plane contributions to the controller contact forces are negligible except for the output shaft assembly weight. It is obvious, given the T_f disagreement, that the shaft bearing contact forces are greater than that estimated in the equation (14) prediction because of small but significant controller misalignment with respect to the rotational plane and radial arm.

The second method was more direct in estimating the dynamic constants for the controller-torsion spring system than the first method. Transient response time-histories were recorded on an oscillograph as the TSC was perturbed by the exciter. By measuring the amplitude decay of the response curves and, additionally, the sinusoidal period, estimates were made of the TSC K, ω_d, and T_f (ref. 9). Table 5 contains the results of the above analysis. There are considerable differences between the T_f values in table 4 and table 5.

From table 4 the average T_f was equal to 0.0226 N-m, whereas the table 5 average estimate was 0.083 N-m, which was almost a 4 to 1 difference. An indication of the accuracy of the second method is seen when a comparison is made of the theoretical versus the experimental values for the system spring constant, K, and for the frequency response, ω_d. The theoretical TSC value when averaged for K is equal to 1.73 N-m/rad and the experimental averaged K is 1.5 N-m/rad, which is an 8.5% difference. The averaged theoretical frequency response (using an empirical system inertia value) is equal to 567 rad/sec whereas the corresponding averaged experimental frequency is 540 rad/sec, which is a 4.8% difference. Because of the difficulties in defining the T_f input parameters of equation (14), a theoretical and experimental comparison cannot be made. However, the table 5 estimates are more likely to be accurate than the table 4 estimates, since satisfactory comparisons were made for K and ω_d. The validity of the assumptions in method 1 is questionable. Still, the inadequate time-history trace resolution probably has resulted in large uncertainties in the T_f values in table 5.

Two important conclusions can be drawn from the above experimental dynamic characteristics analysis. First, it is feasible to adequately measure the high-frequency output-shaft dynamic oscillations of a constant moment controller using a Hall-effect transducer and standard acquisition and recording instrumentation. It is also, therefore, feasible to acquire free-tip dynamic response data by using this instrumentation. Second, basic analysis techniques have been defined and verified to estimate controller (and free-tip) dynamic coefficients, assuming that the response characteristics are those of an approximately single degree of freedom, constant coefficient, second-order differential equation.

CONCLUSIONS

In order to properly evaluate the free-tip-rotor concept, a satisfactory design for a constant moment controller was required. Four designs were tested and evaluated for the FTR application: (1) dual cam controller--cam CF drives the output shaft pin, resulting in control moment; (2) mass-on-string (pulley version)--a kevlar chord and pulley arrangement where the chord tension applies the moment; (3) mass-on-string (cam version)--same operating principle as the above except for the replacement of the pulley by a cam; (4) torsion strap controller--a twisted strap set unwinds under CF loading to produce the required control moment.

The results of the whirl test made the selection of a suitable controller design possible for the FTR evaluation. The controller test results were: (1) dual cam controller--(a) a complex design that was hard to assemble and maintain; (b) scarring on the cam housing surfaces indicated high-friction loads on the cams; (c) large contact forces on the pin and cam slots manifested by localized plastic yielding; (d) analytical models substantially overpredict controller torque output at centrifugal loads greater than 30% of that anticipated at full-scale rotor-tip speeds; (e) empirical evidence indicates the design has inadequate space available for the additional mass required to meet the design torque output goal. (2) Mass-on-string (pulley version)--(a) analytical models overpredict controller torque output, but to a lesser extent than does the DCC; (b) empirical evidence indicates that the design does have sufficient space for the mass required to meet the torque output goals; (c) the design demonstrated a problem with kevlar-chord fatigue and abrasion. (3) Mass-on-string (cam version)--(a) there were critical assembly problems with the design; (b) the controller produced little measurable torque output; no test data were acquired. (4) Torsion strap controller--(a) the controller was a simple design and easy to assemble; (b) analytical models overpredicted the torque output; however, a semiempirical model demonstrated satisfactory agreement with the experimental data; (c) strap pretwist limits prevented testing the controller to meet the design torque output goal; however, the pretwist limit was unique to the controller whirl tested. The overall design concept was considered capable of meeting the goal.

Given the above results, the TSC was selected for the model rotor test of the free-tip rotor.

In addition to the constant moment controller evaluations, instrumentation and analysis techniques were defined and tested for the whirl test that are applicable to free-tip rotor testing. These experimental tools are particularly important for free-tip dynamic response measurements.

APPENDIX A

Dual Cam Controller

Referring to figure 4(b), it can be seen that for the theta-independent case, the DCC torque output is governed by the following equation

$$T = r_s F$$

F is the resultant contact force at the pin/cam interface that is due to the centrifugal load of the cam itself

$$F = \frac{r_{cg}}{r_c} CF$$

$$= \frac{r_{cg}}{r_c} m\Omega^2 R_m$$

where, for simplicity, m is the total mass of both cams. Therefore, the expression for the controller torque output, for the theta-independent case, is

$$T = \frac{1}{r_c} m\Omega^2 R_m r_{cg} r_s \tag{A1}$$

The DCC torque output model can be extended to account for output shaft pitching and for torque variation by noting: (1) as θ changes, the cam c.g. radial location also changes, resulting in a variation of CF and torque; (2) as θ changes, there is a change to the cam moment arm length, r_c, caused by the shaft pins shifting position in the cam slot; (3) as θ changes, there is a change in the radius, r_s, as the pin tends to rotate its way out of the cam slot; and (4) only components of the cam CF and pin contact force contribute to the cam moment balance (these force components are dependent upon ϕ and θ).

The first DCC torque variation contribution (the cam c.g. position shift) can be accounted for by replacing the CF term in equation (A1) by the expressions shown below.

$$CF = m\Omega^2 (R_m + x)$$

$$x = r_{cg} \sin \phi$$

where x is the cam c.g. translation distance (fig. 4(c)). To complete the definition of x it is necessary to obtain an expression for ϕ, the cam angular displacement. As shown in figure 4(b), a point that is coincident on both the shaft

24

and cam planes of rotation must describe an equivalent arc length in both planes as the shaft displaces an angle θ and the cam an angle ϕ. Therefore,

$$r_c \tan \phi = r_s \tan \theta$$

or

$$\phi = \tan^{-1}\left(\frac{r_s}{r_c} \tan \theta\right)$$

(Note that the ratio r_s/r_c demonstrates a gearlike aspect to specifying the relative displacements of these two DCC components.)

The variations in r_c and r_s caused by θ displacement are related by the simple trignometric expressions

$$r_{xc} = \frac{r_c}{\cos \phi}$$

$$r_{xs} = \frac{r_s}{\cos \theta}$$

where r_{xc} and r_{xs} are the moment arm lengths as a function of θ, and where r_c and r_s are the undisplaced lengths (as measured at $\theta = 0$).

The final solution of the DCC theta-dependent model can be performed by applying the moment equilibrium equation to the cam and the shaft. Considering first the cam: only the tangential CF component contributes to the cam moment, and that component is

$$CF_t = CF \cos \phi$$

Next, by applying the moment equation about the cam pivot, the cam/pin contact force, F, can be determined

$$M_{CAM\ PIVOT} = 0$$

or

$$Fr_{xc} = CF_t r_{cg}$$

and therefore

$$F = CF_t \frac{r_{cg}}{r_{xc}}$$

However, it should be noted that it is only a component of F that actually contributes to the shaft torque. Referring to the cam frame of reference, it is only the normal component of F that is perpendicular to the shaft axis and thereby applies the torque. After, defining

$$F_N = F \cos \phi$$

the above two equations can be set equal to each other and results in the expression

$$\frac{F_N}{\cos \phi} = CF_t \frac{r_{cg}}{r_{xc}}$$

$$= m\Omega^2(R_m + x)\cos \phi \frac{r_{cg}}{r_{xc}}$$

or

$$F_N = m\Omega^2(R_m + x)\cos^2 \phi \frac{r_{cg}}{r_{xc}}$$

Finally, only a component of the contact force components, F_N, contributes to the shaft torque. A moment equation applied at the shaft axis

$$M_{SHAFT} = 0$$

gives the following expression for the DCC torque output.

$$T = (F_N \cos \theta)r_{xs}$$

Next, substituting into the torque expression the relationship derived for F_N gives

$$T = m\Omega^2(R_m + x)\cos \theta \cos^2 \phi r_{cg} \frac{r_{xs}}{r_{xc}}$$

Substitution of the expressions for r_{xs} and r_{xc} completes the solution for the DCC control moment. For the theta-dependent case, the torque expression is

$$T = \frac{1}{r_c} m\Omega^2(R_m + x)r_{cg}r_s \cos^3 \phi \qquad \text{(A2a)}$$

where

$$x = r_{cg} \sin \phi \qquad \text{(A2b)}$$

$$\phi = \tan^{-1} \left(\frac{r_s}{r_c} \tan \theta \right) \qquad \text{(A2c)}$$

Note that for the whirl test configuration

$$\theta = \theta_0 - T/K_S \qquad \text{(A2d)}$$

where θ_0, K_S, and T are the initial shaft angle without the application of torque, the resisting spring constant, and the controller output torque, respectively. This spring deflection constraint must be applied to the torque output equation set in order to compare analytical predictions with the whirl test data.

One of the performance constraints of the free-tip controller is the requirement that the torque output variation should be less than 10% of the nominal value while varied within a ±10° pitch range. The next expression to be developed will provide an estimate of the DCC percent torque variation, and will therefore show whether or not the prototype violates the constraint.

Let T_0 be the torque estimate of equation (A1), and let T_1 be the torque estimate of equation (A2) at some arbitrary θ. Therefore

$$\delta = \frac{T_1 - T_0}{T_0} \times 100\% \qquad \text{(A3a)}$$

making the proper substitutions

$$\delta = \frac{r_{cg}}{R_m} \sin \phi \cos^3 \phi \qquad \text{(A3b)}$$

where ϕ is defined in equation (A2c).

Using the DCC prototype input parameters in table 1 and a maximum θ deflection of 10° the above equation results in $\delta = 0.25\%$, excluding friction effects. The DCC conceptually satisfies the design constraints.

Mass-on-String

The second controller to be modeled is the MOS. Again, as in the DCC, two models will be developed for the theta-independent and dependent assumptions.

Figure 5(b) is a simple free-body diagram of the controller in its undisplaced position, for a given shaft angle. It can be seen from this figure that the MOS torque output for the theta-independent case is

$$T = CFr_s$$

then

$$T = m\Omega^2 R_m r_s \qquad (A4)$$

Referring to figure 5(b) for the kinematic diagram of the MOS controller as it is displaced from its initial position, it can be seen that the only means by which the torque can vary is by the translation of the controller's active mass as the shaft angle changes: i.e., mass translation in the radial direction results in a varying R_m, which in turn results in a varying CF and torque. In order to extend the MOS torque expression to incorporate this mass translation factor, it is necessary only to replace the parameter R_m in equation (A4) with the variable expression $(R_m + x)$, where R_m is defined as before and where x is the translation distance. Therefore, the torque output is now a variable quantity that is dependent on x, and so is therefore dependent upon the controller shaft pitch angle, θ. Therefore,

$$T = m\Omega^2 (R_m + x)r_s$$

The relationship between θ and x is illustrated in figure 5(b). It is found that

$$T = m\Omega^2 [R_m + \theta r_s]r_s \qquad (A5)$$

Equation (A5) is therefore the theta-dependent MOS model. The MOS ideal torque variation (δ) is then

$$\delta = \theta r_s \times 100\% \qquad (A6)$$

The variation in torque is ±0.18% of the nominal value for 20° of shaft θ deflection and for the table 2 input parameters of the whirl-tested MOS prototype. Again, this controller is conceptually well within the design constraint.

The torque output model (theta-dependent) can be modified to agree with the experimental configuration used during the whirl test. The resisting-spring θ constraint needs to be incorporated into the analytical model so as to compare the model predictions with the whirl-test data. Substituting equation (A2d) into equation (A5) and solving for the torque results in

$$T = \frac{m\Omega^2 R_m r_s}{[1 - (r_s^2/K_s)m\Omega^2]} \qquad (A7)$$

Torsion Strap Controller

The TSC model for both cases, theta-independent and theta-dependent as applied to the whirl-test apparatus, is essentially the same. The only difference is the application of different θ conditions. For the theta-independent case, $\theta = \theta_{PT}$, and for the theta-dependent case, $\theta = \theta_{PT} + \Delta\theta$ where θ_{PT} is the torsion strap pretwist angle.

The analysis derives torque output equations for the TSC. It assumes that the torsional elastic properties of the mechanism to be negligible and considers only rigid body mechanics. The analysis also makes three additional simplifying assumptions: the strap length and strap width are not a function of the strap tensile loading, and the strap width (which is twice the moment arm length) does not vary along the length of the strap. All three geometry changes occur, however, with the TSC pretwisted and loaded under tension. The experimental results section notes that these small geometry changes will have a major influence on the torque output predictions.

As can be seen in figure 7(b), the torque output is the consequence of a normal force couple, $\pm F_N$, as it is applied about the strap moment arm, r. Therefore

$$T = F_N r$$

Referring to the incremental strap segment shown in figure 7(b), the force F_N is seen to be a component of the centrifugal force that is applied to the twisted torsion strap. Therefore, as per the strap free-body diagram

$$CF = F_T \cos \phi$$

or rearranged as

$$F_T = \frac{CF}{\cos \phi}$$

and

$$F_N = F_T \sin \phi$$

Combining the above equations the TSC torque output is

$$T = rCF \tan \phi$$

The strap twist angle, ϕ, is dependent upon the magnitude of θ and on the strap geometry, r and l. Additionally, as the free end of the torsion strap is twisted, it will describe a geometric arc in space. The arc length is another parameter that is important in defining ϕ. If the assumption is made that the strap slope for a given pitch angle is constant, then trigonometric identities can be related to the slope, to the arc length of the twisted strap, and to the strap length. These parameters can be thought of as an angle and as line segments being

mapped upon a cylindrical surface, forming a triangle. The resulting geometric relationship is

$$\tan \phi = \frac{x}{1}$$

or

$$\phi = \tan^{-1} \frac{x}{1}$$

where x is the arc length described by a point on the shaft that is rotated by $\theta°$. Therefore

$$x = \theta r$$

Given the information provided and making the appropriate substitutions, the model governing equations are therefore

$$T = rm\Omega^2 R_m \tan \phi \qquad (A8a)$$

$$\phi = \tan^{-1} \left(\frac{\theta r}{1} \right) \qquad (A8b)$$

where for the whirl-test prediction comparisons, a special case of the theta-dependent condition is applied, i.e.,

$$\theta = \theta_{PT} - T/K_S$$

30

Dual Cam Controller

Since equations (1) and (2) are to be used for comparison with the experimental results of the DCC, it is necessary to get an estimate of the uncertainty in the model's predictions. The following uncertainty analysis is based on work in reference 7. It is a statistical method that estimates the uncertainty of a calculated parameter, within a certain probability.

Because there is little difference between the results of the two DCC torque expressions, an uncertainty analysis is performed only on the simple model, equation (1). The first step in the analysis is the calculation of all of the partial derivatives of the calculated parameter with respect to the measured parameters.

The torque has the functional form

$$T = T(m, \Omega, R_m, r_{cg}, r_s, r_c)$$

The derivatives are

$$\frac{\partial T}{\partial m} = \frac{1}{r_c} \Omega^2 R_m r_{cg} r_s \tag{B1a}$$

$$\frac{\partial T}{\partial \Omega} = \frac{2}{r_c} m\Omega R_m r_{cg} r_s \tag{B1b}$$

$$\frac{\partial T}{\partial R_m} = \frac{m\Omega^2 (r_{cg}) r_s}{r_c} \tag{B1c}$$

$$\frac{\partial T}{\partial r_{cg}} = \frac{m\Omega^2 R_m r_s}{r_c} \tag{B1d}$$

$$\frac{\partial T}{\partial r_s} = \frac{m\Omega^2 R_m (r_{cg})}{r_c} \tag{B1e}$$

$$\frac{\partial T}{\partial r_c} = \frac{m\Omega^2 R_m (r_{cg}) r_s}{r_c^2} \tag{B1f}$$

The second step in the prediction uncertainty analysis is an estimate of the accuracy of the measured parameters. There is a 95% probability that the actual parameter magnitude should fall within its specified accuracy range as this

confidence level was chosen for the torque output prediction uncertainties as they were calculated in this appendix. Refer to table 1 for the dual cam's estimated measurement accuracies. In addition to instrumentation sensitivity, measured parameter accuracies take into account difficulties in defining controller component c.g. locations and nominal dimensions under centrifugal loading. Given the table 1 parameter values, prediction uncertainty estimates were calculated and discussed in the experimental results section.

The final step to the uncertainty analysis is the evaluation of the following equation which is the square root of the summation of the squares of the products of the partial derivatives and the estimated inaccuracies of all of the measured parameters

$$\omega_T = \sqrt{\sum_{i=1}^{N} \left(\frac{\partial T}{\partial x_i} \omega_i \right)^2} \qquad (B2)$$

which for this particular case results in

$$\omega_T = \left[\left(\frac{\partial T}{\partial m} \omega_m \right)^2 + \left(\frac{\partial T}{\partial \Omega} \omega_\Omega \right)^2 \cdots + \left(\frac{\partial T}{\partial r_c} \omega_{r_c} \right)^2 \right]^{1/2} \qquad (B3)$$

where ω is an accuracy estimate and its subscript references the measured parameter. It should be noted that the confidence of the uncertainty estimate for the torque is the same as that for the measured parameters, 95%.

Mass-on-String

To calculate the uncertainty of the theta-independent MOS torque output model predictions, note that

$$T = T(m, \Omega, R_m, r_s)$$

Therefore, based on equation (6) the required partial derivatives are

$$\frac{\partial T}{\partial m} = \Omega^2 R_m r_s \qquad (B4a)$$

$$\frac{\partial T}{\partial \Omega} = 2m\Omega R_m r_s \qquad (B4b)$$

$$\frac{\partial T}{\partial R_m} = m\Omega^2 r_s \qquad (B4c)$$

32

$$\frac{\partial T}{\partial r_s} = m\Omega^2 R_m \qquad\qquad (B4d)$$

The measured parameters' accuracies are listed in table 2. By substituting in these values, the theta-independent torque output model uncertainty is estimated by using equations (B2) and (B4).

Equation (7b) accounts for the influence of the spring deflection on the theta-dependent MOS torque output. In functional form, therefore

$$T = T(m, \ \Omega, \ R_m, \ r_s, \ K_S)$$

Performing the uncertainty analysis, the partial derivatives are

$$\frac{\partial T}{\partial m} = \frac{\Omega^2 R_m r_s}{[1 - (r_s^2/K_S)m\Omega^2]^2} \qquad\qquad (B5a)$$

$$\frac{\partial T}{\partial \Omega} = \frac{2mR_m r_s \Omega}{[1 - (r_s^2/K_S)m\Omega^2]^2} \qquad\qquad (B5b)$$

$$\frac{\partial T}{\partial R_m} = \frac{m\Omega^2 r_s}{[1 - (r_s^2/K_S)m\Omega^2]} \qquad\qquad (B5c)$$

$$\frac{\partial T}{\partial r_s} = \frac{m\Omega^2 R_m [1 + (1/K_S)m\Omega^2 r_s^2]}{[1 - (r_s^2/K_S)m\Omega^2]^2} \qquad\qquad (B5d)$$

$$\frac{\partial T}{\partial K_S} = \frac{-m^2 \Omega^4 r_s^3 R_m}{K_S^2 [1 - (r_s^2/K_S)m\Omega^2]^2} \qquad\qquad (B5e)$$

To complete the prediction model uncertainty analysis, the above partial derivatives and the accuracy estimates of table 2 are substituted into equation (B2).

Torsion Strap Controller

The functional form of the TSC torque solution, for the uncertainty analysis, is

$$T = T(r, \ m, \ \Omega, \ R_m, \ \theta_{PT}, \ K_S, \ 1)$$

By applying the spring deflection constraint, the TSC torque output is no longer analytically solvable. The implicit nature of the constrained TSC torque

output model prevents an analysis of the partial derivatives that are necessary for this prediction uncertainty. Therefore an algorithm was devised to numerically approximate these derivatives. Using first-order finite-difference expressions, the derivative calculations were based upon iterative solutions of the torque output for a converging interval about each specified parameter's nominal value, whereas all other parameters retained their nominal value.

Table 3 presents the TSC parameter accuracy estimates used in the torque uncertainty calculations.

APPENDIX C

Controller inertia expressions are derived by an equivalent kinetic energy approach (ref. 8). Essentially, the system inertia is found by use of the following relationship

$$KE_{SYSTEM} = KE_{COMPONENTS}$$

or, more specifically for the controller prototypes

$$\frac{1}{2} I_e \left(\frac{d\theta}{dt}\right)^2 = \frac{1}{2} \sum_{i=1}^{N} I_i \left(\frac{d\theta_i}{dt}\right)^2 + \frac{1}{2} \sum_{i=1}^{N} m_i V_i^2 \tag{C1}$$

This relationship defines an equivalent mechanism that has the same output angular velocity and inertia as does the original mechanism, but which is described by a second-order dynamic system.

Dual Cam Controller

Referring to figure 4(b), it can be seen that application of equation (C1) to the DCC prototype results in the following expression

$$\frac{1}{2} I_e \left(\frac{d\theta}{dt}\right)^2 = \frac{1}{2} I_{FT} \left(\frac{d\theta}{dt}\right)^2 + \frac{1}{2} I_s \left(\frac{d\theta}{dt}\right)^2 + \frac{1}{2} I_e \left(\frac{d\phi}{dt}\right)^2$$

The second angular velocity term $d\theta_2/dt$ is the cam velocity. Cam velocity can be related to the shaft velocity by the expression

$$\frac{d\phi_2}{dt} = \frac{r_s}{r_c} \frac{d\theta}{dt}$$

The system inertia for the DCC is

$$I_e = I_{FT} + I_s + I_c \left(\frac{r_s}{r_c}\right)^2 \tag{C2}$$

It should be noted that the above equation assumes that the cable restraining the output shaft does not significantly stretch under centrifugal loading. If the cable stretch is not negligible, the result would be an effective shift in the r_c

for each of the pin interfaces. Taking cable stretch into account in the system inertia estimate of the DCC results in the following modified expression

$$I_e = I_{FT} + I_s + \frac{1}{2} I_c \left[\frac{r_{xs}}{r_{xc} - d} \right]^2 + \frac{1}{2} I_c \left[\frac{r_{xs}}{r_{xc} + d} \right]^2 \tag{C3}$$

where d is the cable displacement in the radial direction. Note that if d = 0 then the equation reduces to that of equation (C2).

Similarly, the kinetic energy approach is used for the MOS (equation (C4)) and the TSC (equation (C5)) controllers:

$$I_e = I_{FT} + I_s + I_p \left(\frac{r_s}{r_p} \right)^2 + mr_s^2 \tag{C4}$$

$$I_e = I_{FT} + I_s \tag{C5}$$

Estimates for the prototypes' spring constants can be derived by considering the controller theta-dependent torque output expressions, equations (2), (7a), and (11). The equations can be linearized and the spring constant can be calculated.

The DCC theta-dependent torque output model can be linearized by a small-angle assumption. The DCC design tested during the whirl test had a θ hard-stop restriction of ±10°. Using equation (2c) and the data in table 1, the ϕ range for the DCC that was tested was ±6°. Both these angles are acceptable for the small-angle approximations used below.

Now the applicable DCC torque output expressions are

$$T = \frac{1}{r_c} m\Omega^2 (R_m + x) r_{cg} r_s \cos^3 \phi$$

$$x = r_{cg} \sin \phi$$

and

$$\tan \phi = \frac{r_s}{r_c} \tan \theta$$

The torque model can be linearized by the following small-angle approximations: $\cos \phi \approx 1$, $\sin \phi \approx \phi$, $\tan \theta \approx \theta$, and $\tan \phi \approx \phi$. The linear model is

$$T \approx m\Omega^2 \left(\frac{r_{cg} r_s}{r_c} \right)^2 \theta \qquad (D1)$$

Therefore, by definition

$$K_{dcc} = m\Omega^2 \left(\frac{r_{cg} r_s}{r_c} \right)^2 \qquad (D2)$$

For the MOS controller, referring to equation (7a)

$$T = m\Omega^2 R_m r_s + [m\Omega^2 r_s^2]\theta$$

results in

$$K_{mos} = [m(\Omega r_s)^2] \qquad (D3)$$

The TSC analytical model, equation (11), is nonlinear. The equation can be simplified by use of the following approximation: $\tan \phi \approx \phi$ for small ϕ.

The TSC expression can then be linearized and has the form:

$$T \approx m(\Omega r)^2 \frac{R_m}{l} \theta \qquad \text{(D4)}$$

Thus

$$K_{tsc} = m(\Omega r)^2 \frac{R_m}{l} \qquad \text{(D5)}$$

APPENDIX E

The major contribution to controller damping is friction. There are two funda-
mental problems with arriving at an estimate of the controllers' damping coefficient
(T_f): (1) arriving at a reasonable normal contact force estimate, and (2) specify-
ing the friction coefficients.

A friction coefficient value is unique to each mechanical system and is not
easily calibrated. There are handbooks containing ranges of μ values for differ-
ent material combinations, but the uncertainty in application is large. Though the
physics of defining an out-of-plane normal force are straightforward, the contact
friction forces are dependent on β, ζ, and mechanism component misalignment--
localized conditions that are not easily defined or measured. If there is misalign-
ment, then scouring could occur prohibiting any damping analysis.

At best, what can be accomplished is an approximate estimate of the magnitude
of T_f, but one where the physics are clearly outlined. The first step to the
solution is the reduction of the torque coulomb damping constant into individual
components. The result is the following expression:

$$T_f = T_{f(shaft)} + T_{f(controller\ active\ elements)}$$
$$+ T_{f(the\ torsional\ spring\ resisting\ component)}$$

The frictional torque from the controller's active elements can be further
subdivided into contributions from individual mechanical elements, and is therefore
unique to each controller that is analyzed. In all four controllers studied, the
frictional torque from the shaft is the same. For this reason this damping compo-
nent will be analyzed first; the unique contributions will be analyzed later.

The shaft friction component can be expressed as $T_{f(shaft)} = \mu r_s N$ where μ,
r_s, and N are the friction coefficient, the shaft radius, and the bearing normal
contact force, respectively.

The normal force, N, must be defined. For this experiment, as the plane of
rotation is assumed to be rigid, there are three contributions to N: the weight of
the controller's active mass, the out-of-plane CF component caused by coning, or
nonzero β, and the in-plane normal CF component caused by lead-lag, or nonzero
ζ. A free-body diagram of these normal force components is shown in figure 13.
These components are vectorally added to arrive at the resultant force, N. The
expression for N is:

$$N = \sqrt{(W \cos \beta)^2 + (CF \sin \beta)^2 + (CF \sin \zeta \cos \beta)^2} \tag{E1}$$

and so the complete expression for the T_f shaft component is:

$$T_{f(shaft)} = \mu r_s \sqrt{(W \cos \beta)^2 + (CF \sin \beta)^2 + (CF \sin \zeta \cos \beta)^2} \qquad (E2)$$

Since the above equation has been developed for the common and the largest friction term for all four prototypes, it is now necessary to derive the additional terms that are due to unique prototype mechanical components. For the TSC controller, equation (E2) is the only friction contribution.

The DCC controller has a single additional T_f term that needs to be derived, i.e., the friction contribution of the cams that come into contact with the controller housing. Referring to figures 14(a) and 14(b), the free-body diagrams illustrate two items necessary for the term $T_{f(dcc)}$. First, each cam has its own normal force component which acts against the controller's housing--this must be estimated. Second, the friction forces will impart a resisting torque to the cam's motion, which in turn applies a torque to the output with its magnitude governed by the mechanical advantage ratio of the cams.

The cam contact force, taking centrifugal out-of-plane components into account, can be expressed as:

$$N_{dcc} = W_{dcc} \cos \beta + CF_{dcc} \sin \beta \qquad (E3)$$

Only the β contribution results in a friction force. The ζ component does not act normal to the cam/housing surface. The cam mechanical advantage ratio as derived earlier was found to be

$$T_{shaft} = F_{cam} \frac{r_{cg} r_s}{r_c} \qquad (E4)$$

In the original equation F_{cam} was the centrifugal force; however, the same relationship is applicable for determining the resisting torque that is due to friction force, since both forces act through the cam's c.g. and the same kinematic linkage.

Therefore, the additional T_f term in DCC is found to be:

$$T_{f(dcc)} = \mu \frac{r_{cg} r_s}{r_c} N_{dcc} \qquad (E5)$$

The above equation assumes that the pitch-angle displacement is small. Given the minor variation in torque output as seen in the dynamic DCC model, this is a suitable approximation.

For the remaining controller, the MOS, the damping estimate can be completed by again noting that the mechanism contact force is still governed by equation (E1), only now with the weight and centrifugal load being that of the translating

mass. Similarly, the transformation of the translating mass friction force to a resisting torque can be found by referring back to the controllers' torque performance equation, in this case equation (6).

Therefore, it is seen that the MOS mass friction contribution is simply

$$T_{f(mos)} = \mu r_s N_{mos} \qquad \text{(E6)}$$

where

$$N_{mos} = \sqrt{(W_{mos} \cos \beta)^2 + (CF_{mos} \sin \beta)^2 + (CF_{mos} \sin \zeta \cos \beta)^2}$$

This completes the equation set for estimating the friction resistance to controller dynamic oscillations. Only the final term, T_f (mechanical spring) is left undefined. The mechanical spring damping is a combination of coulomb and strain energy damping. The friction contribution is undefinable because the load path of the mechanical spring cannot be directly analyzed. The strain energy dissipation term can only be empirically determined.

REFERENCES

1. Hooper, W. E.: The Vibratory Airloading of Helicopter Rotors. Ninth-European Rotorcraft Forum, Stresa, Italy, Paper No. 46, Sept. 1983.

2. Stroub, Robert H.: Performance Improvements with the Free-Tip Rotor. AHS National Specialists' Meeting, Rotor System Design, Oct. 1980.

3. Stroub, Robert H.: A Constant Lift Rotor for a Heavier Than Air Craft. U.S. Patent 4,137,010, Jan. 30, 1979.

4. McVeigh, M. A.; Rosenstein, H.; Bartie, K.; and McHugh, F. J.: Investigation of a Rotor System Incorporating a Constant-Lift Tip. (Boeing Vertol Co.; NASA Contract NAS2-10769) NASA CR-166361, 1981.

5. Stroub, Robert H.: An Experimental Investigation of a Free-Tip Rotor Configuration in a Forward Flight Wind-Tunnel Test. NASA TM-84409, 1983.

6. Tipler, P. A.: Physics. Worth Publishers, Inc., 1976.

7. Holman, J. P.; and Gajda, Jr., W. J.: Experimental Methods for Engineers, Third ed., McGraw-Hill, 1978.

8. Shigley, J. E.: Mechanical Engineering Design. Third ed., McGraw-Hill, 1977.

9. Vierck, R. K.: Vibration Analysis. Second ed., Harper and Row, 1979.

TABLE 1.- DCC DESIGN GEOMETRY AND OPERATING CONDITIONS

Dual cam parameter accuracies		
Parameter	Nominal value x_i	Accuracy ω_{x_i}
m	0.039 kg	$\pm 4.08 \times 10^{-3}$ kg
R_m	.8 m	$\pm 1.3 \times 10^{-2}$ m
r_c	8.45×10^{-3} m	$\pm 1.588 \times 10^{-3}$ m
r_{cg}	1.88×10^{-2} m	$\pm 1.588 \times 10^{-3}$ m
r_s	5.08×10^{-3} m	$\pm 8.128 \times 10^{-4}$ m
Ω	Variable	$\pm .5$ rad/sec

TABLE 2.- MOS DESIGN GEOMETRY AND OPERATING CONDITIONS

MOS parameter accuracies		
Parameter	Nominal value x_i	Accuracy ω_{x_i}
K_S	0.0395 N-m/deg	$\pm 5.65 \times 10^{-3}$
m	.045 kg	$\pm 6.8 \times 10^{-3}$ kg
R_m	.813 m	$\pm 2.54 \times 10^{-2}$ m
r_s	5.08×10^{-3} m	$\pm 7.62 \times 10^{-4}$ m
Ω	Variable	$\pm .5$ rad/sec

TABLE 3.- TSC DESIGN GEOMETRY AND OPERATING CONDITIONS

TSC parameter accuracies		
Parameter	Nominal value x_i	Accuracy ω_{x_i}
K_S	0.0395 N-m/deg	$\pm 5.65 \times 10^{-3}$
l	.0667 m	$\pm 3.175 \times 10^{-3}$ m
m	.288 kg	$\pm 4.54 \times 10^{-3}$ kg
M_r	1.052 m	$\pm 1.27 \times 10^{-2}$ m
r	5.08×10^{-3} m	$\pm 7.62 \times 10^{-4}$ m
Ω	Variable	$\pm .5$ rad/sec
θ_0	Experimental values: 17°, 47°, 67°, 89°	$\pm 10\%$ nominal

PITCH
AXIS

CONTROL
MOMENT

LIFT
FORCE

SELF ADJUSTING
BLADE PITCH

LIFT

M_c'

PITCH AXIS AND
CENTER OF GRAVITY
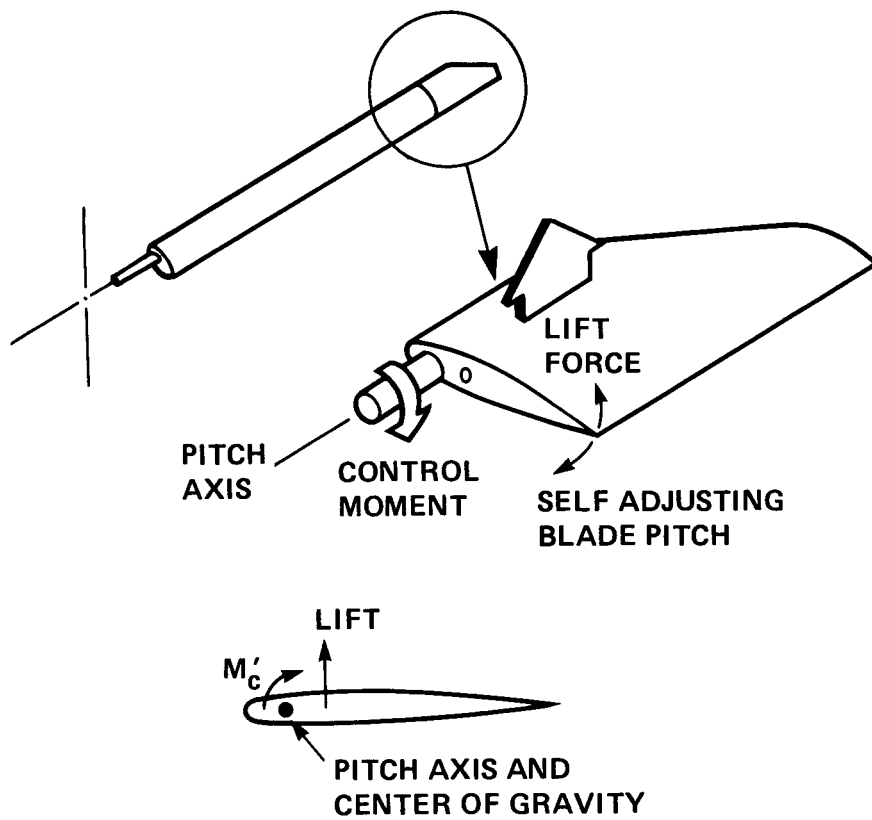
Figure 1.- The Free-tip-rotor concept.

44
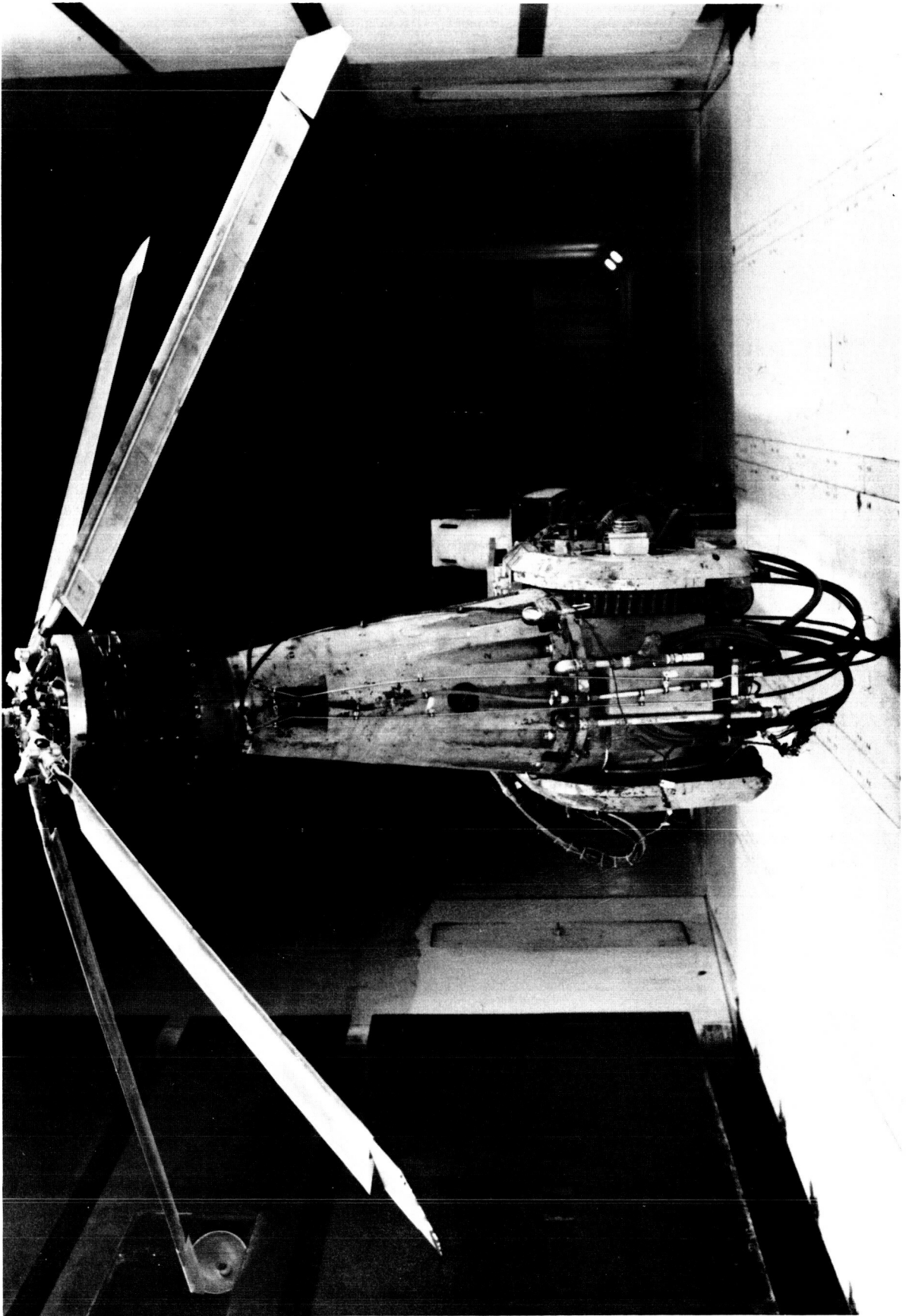
Figure 2.- Free-tip rotor.
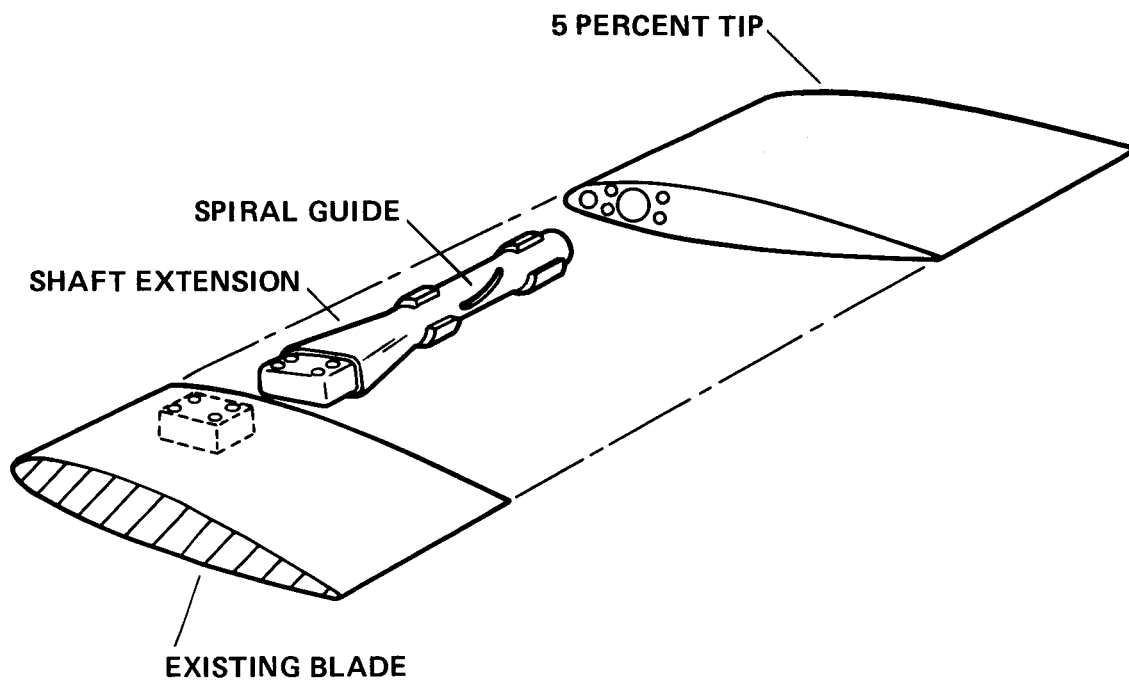
Figure 3.- First-constant-moment-controller design.

VIEW A–A
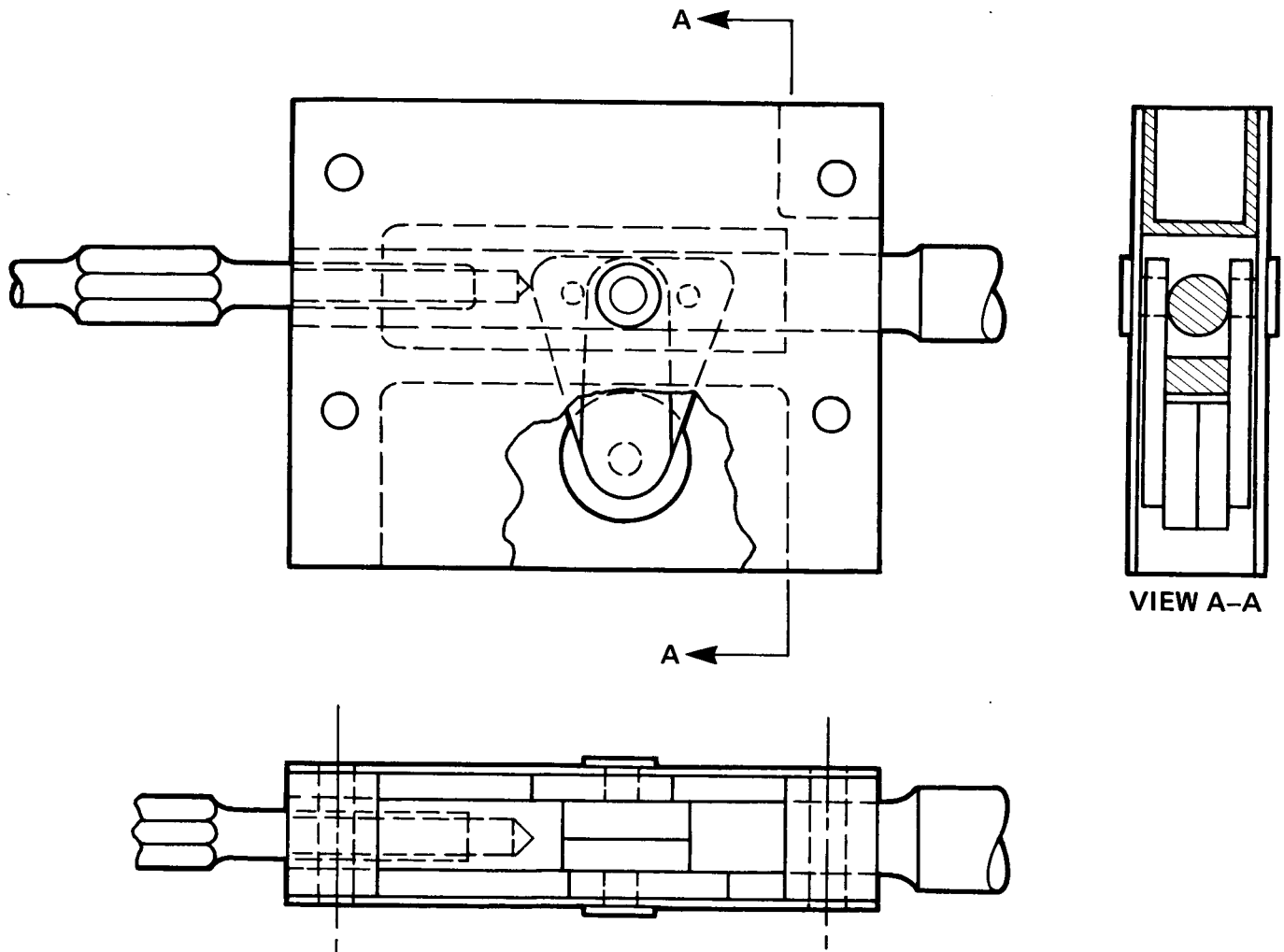
(a) Assembly.

Figure 4.- Dual cam controller.
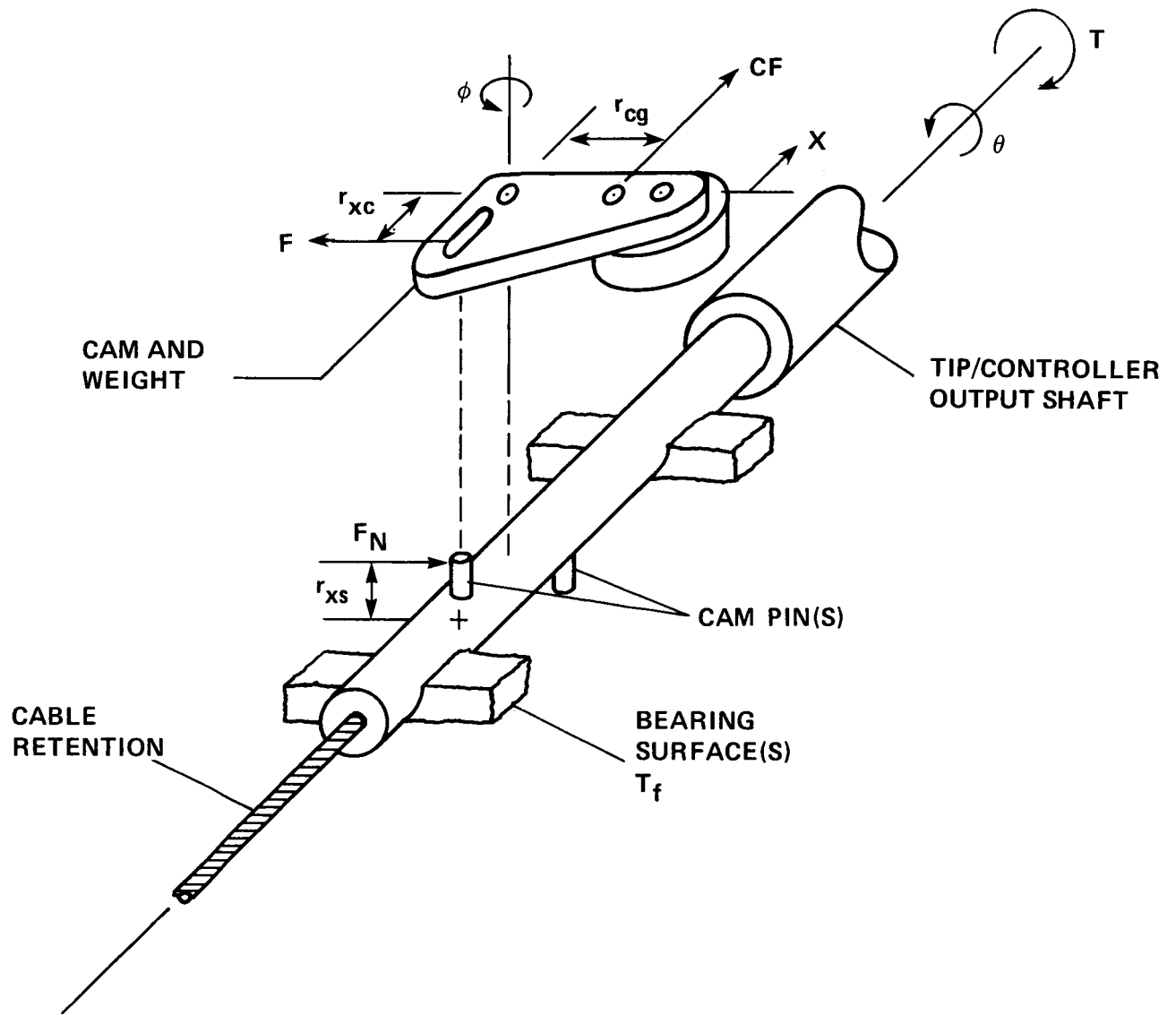
(b) Free-body.

Figure 4.- Concluded.
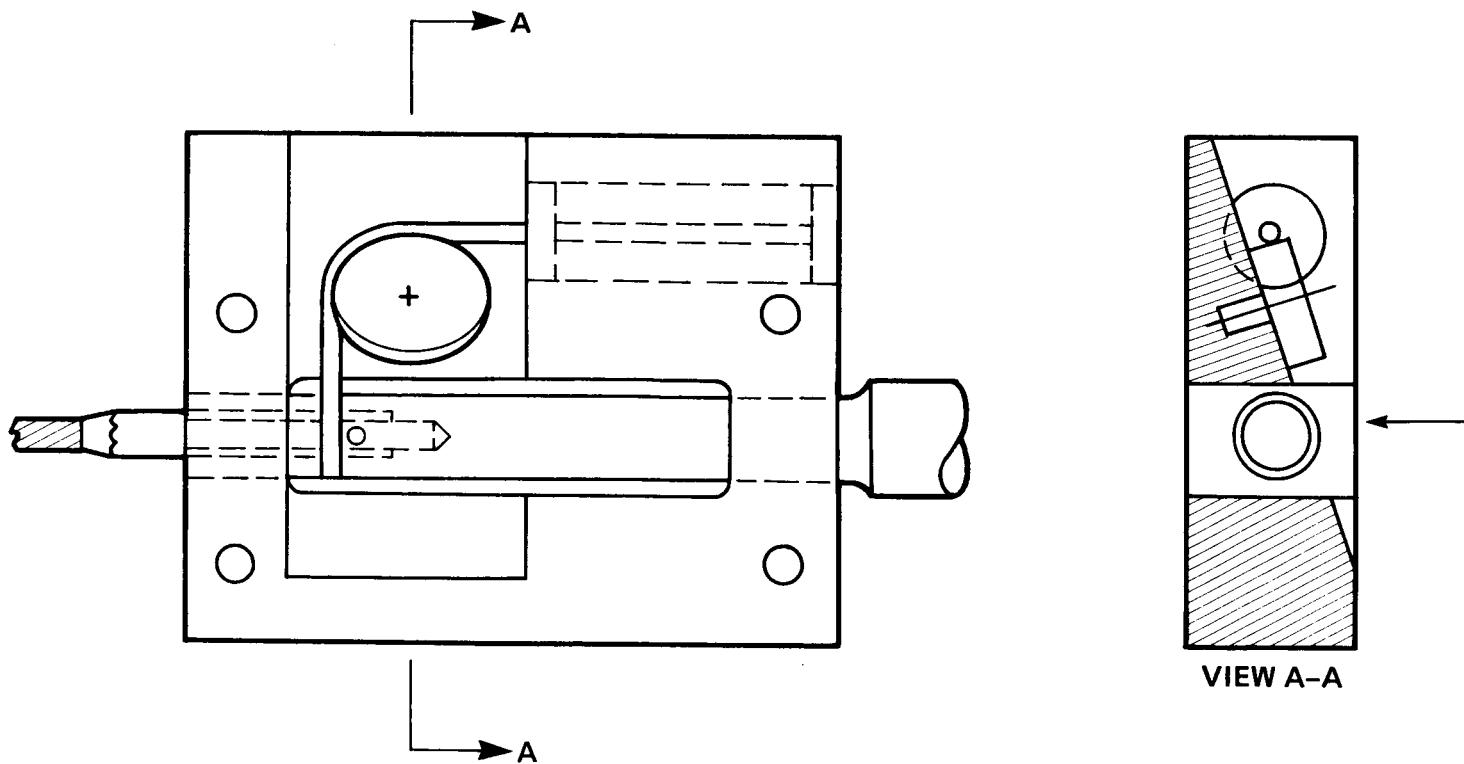
(a) Assembly.

Figure 5.- Mass-on-string (pulley version).

BEARING SURFACE(S)

CONTROLLER
OUTPUT SHAFT

VIEW A - A
2 X SCALE

F

r

θ

A

A

F = CF

F = -CF

CABLE RETENTION

BONDED
KEVLAR
CABLE

PULLEY

r_p

ϕ

R_m

X

CF

m
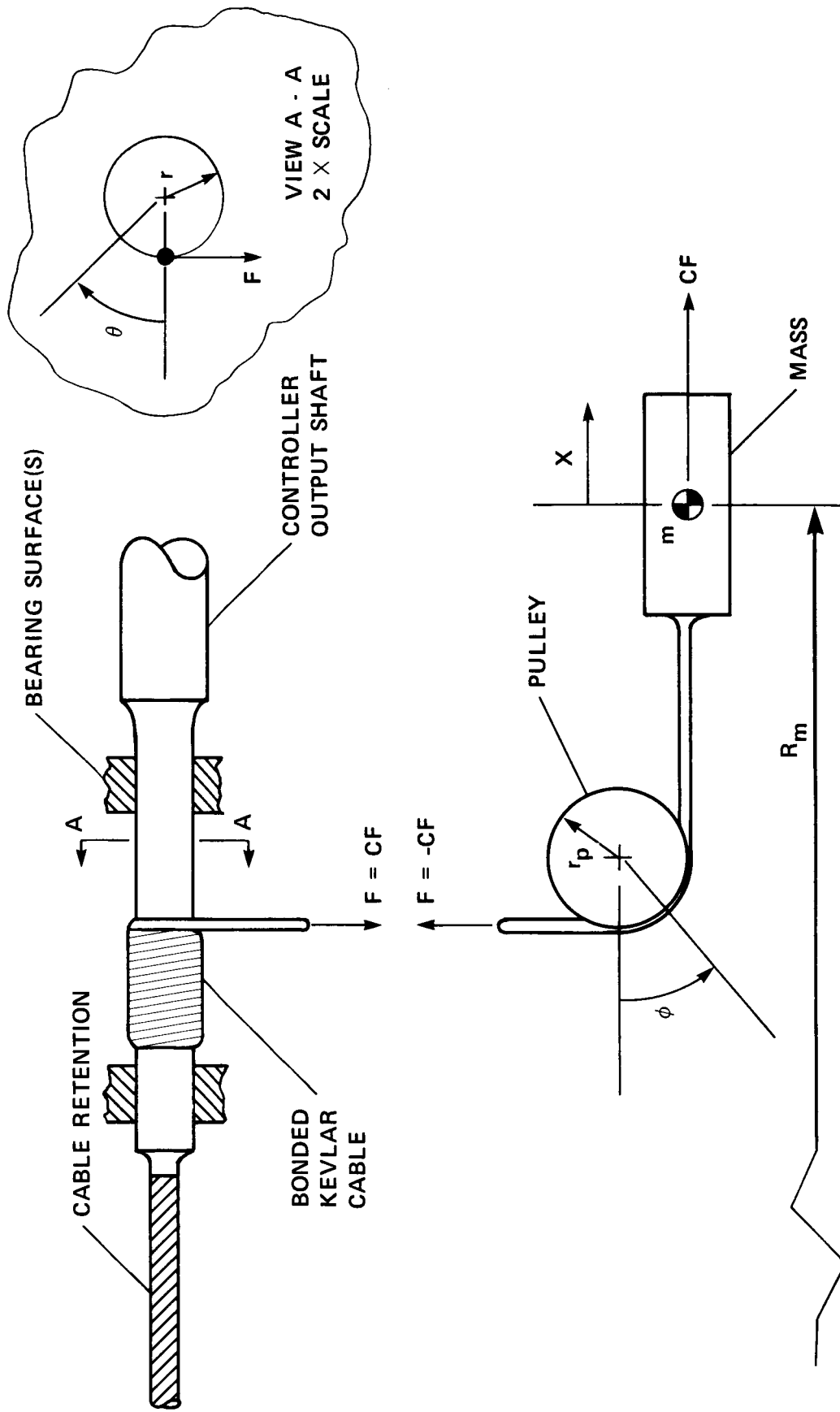
MASS

(b) Free-body.

Figure 5.- Concluded.
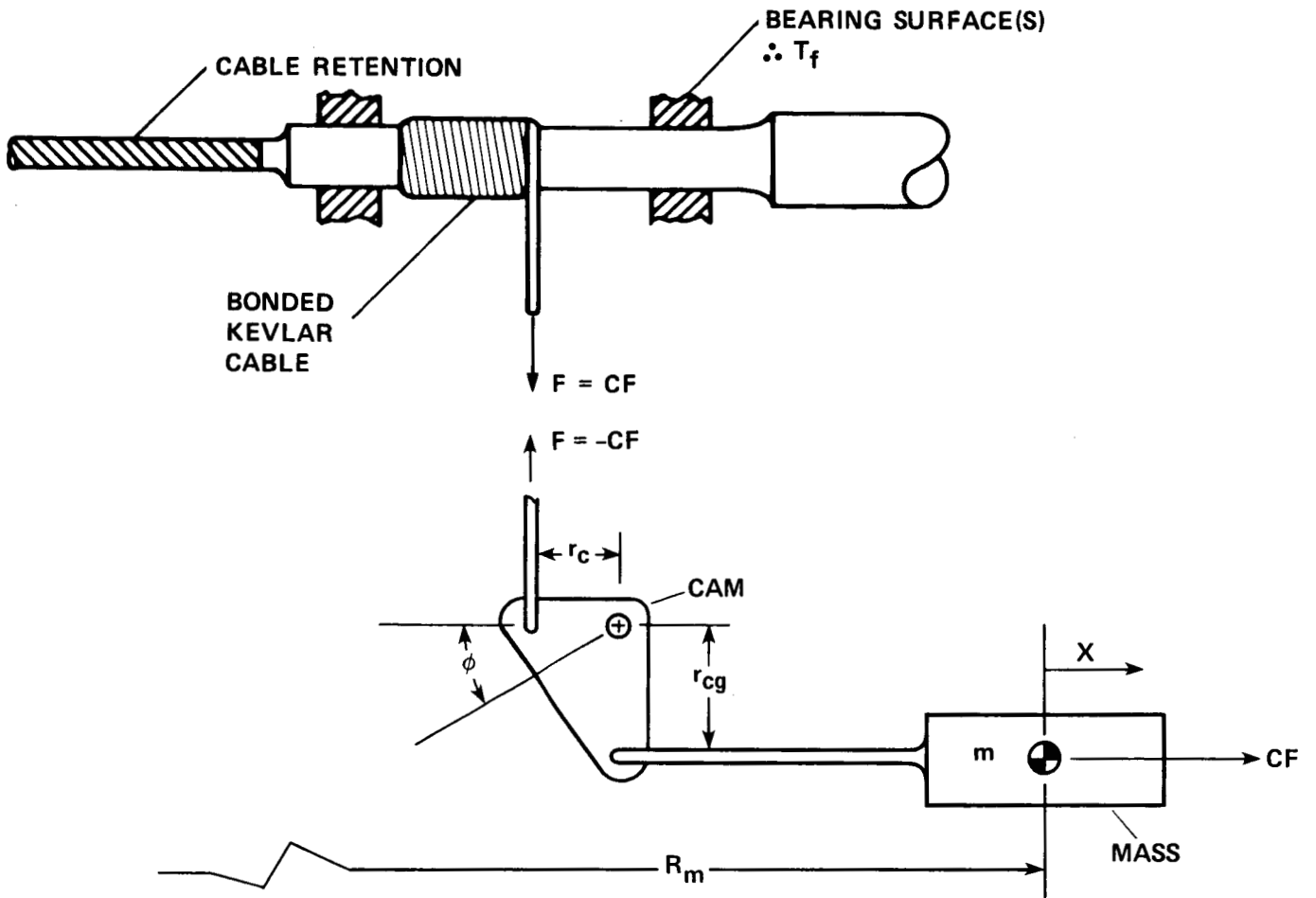
Figure 6.- Mass-on-string (cam version).
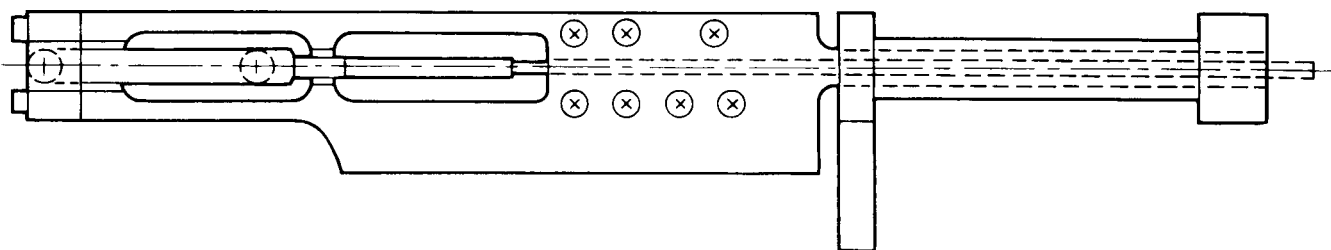
(a) Assembly.

Figure 7.- Torsion strap controller.
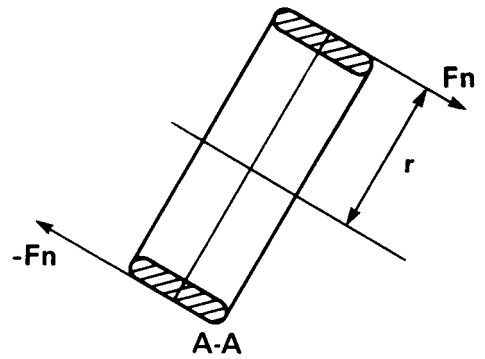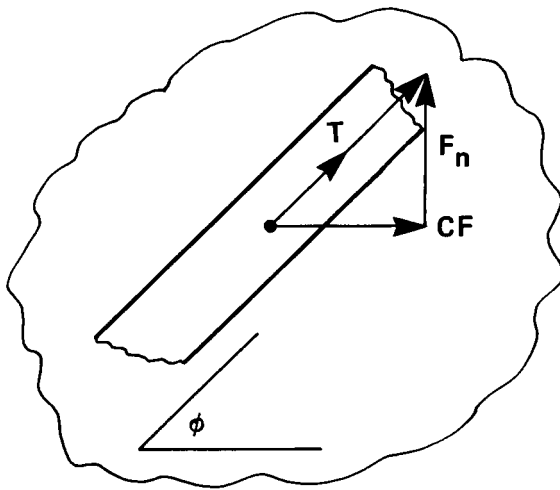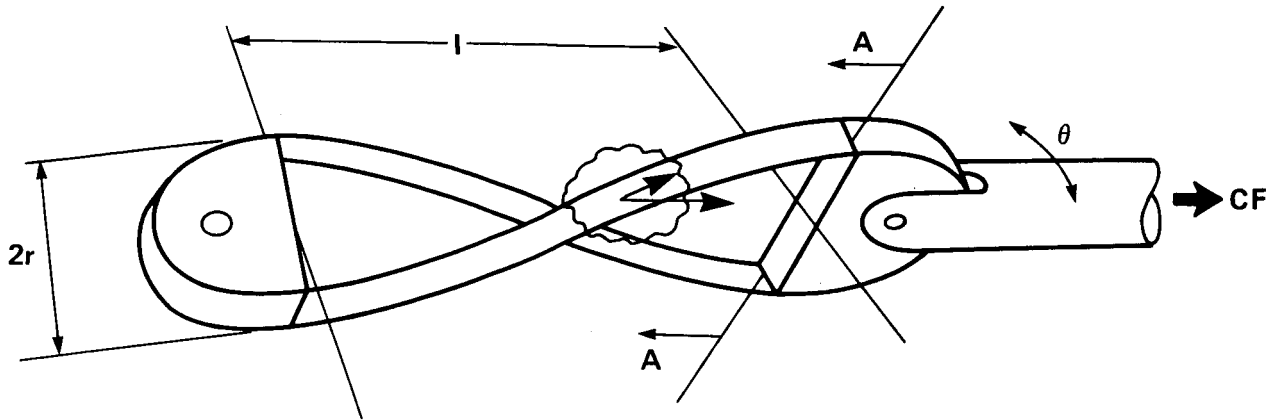
(b) Free-body.

Figure 7.- Concluded.

Figure 8.- Whirl rig.

ELECTRIC MOTOR DRIVEN
EXCITOR WITH CAM

WHIRL RIG
TEST BED

CONTROLLER PROTOTYPE
WITH TRIP LEVER AND
SPRING ASSEMBLY

Ω
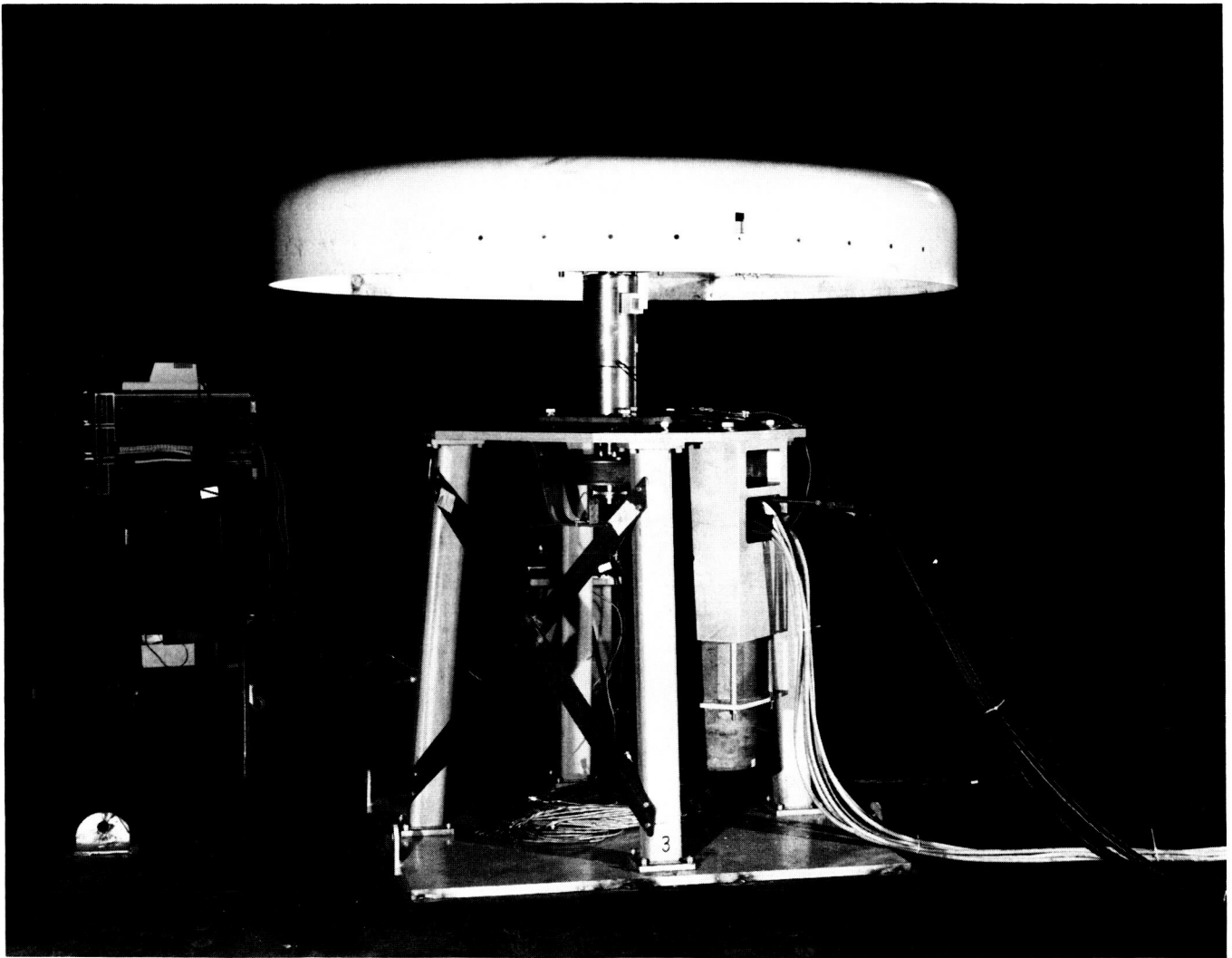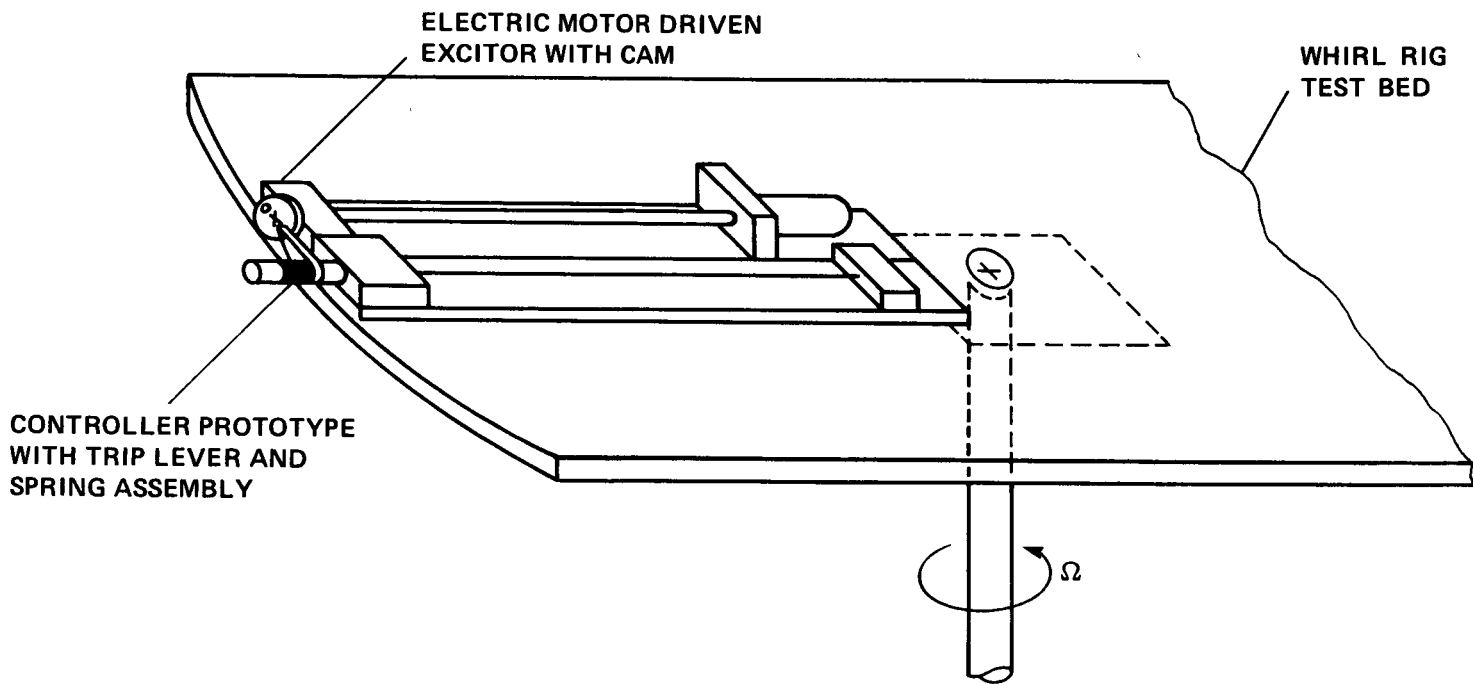
Figure 9.- Controller test bed.
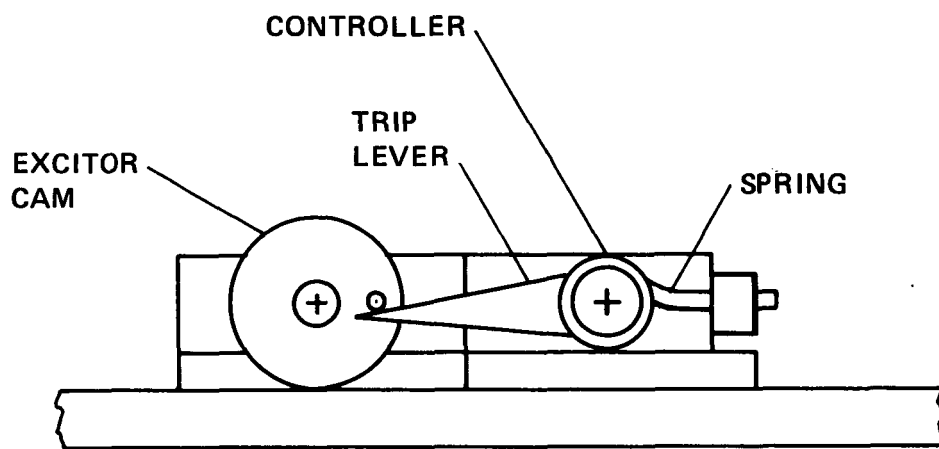
Figure 10.- Exciter and controller assembly.

CONTROLLER
MODULE

$\Delta\theta$

TRIP
LEVER

OPPOSING TORQUE
MECHANICAL SPRING

DETACHABLE
CABLE-PULLEY
CALIBRATION
FIXTURE

W (WEIGHTS IMPOSE
CALIBRATION TORQUE)
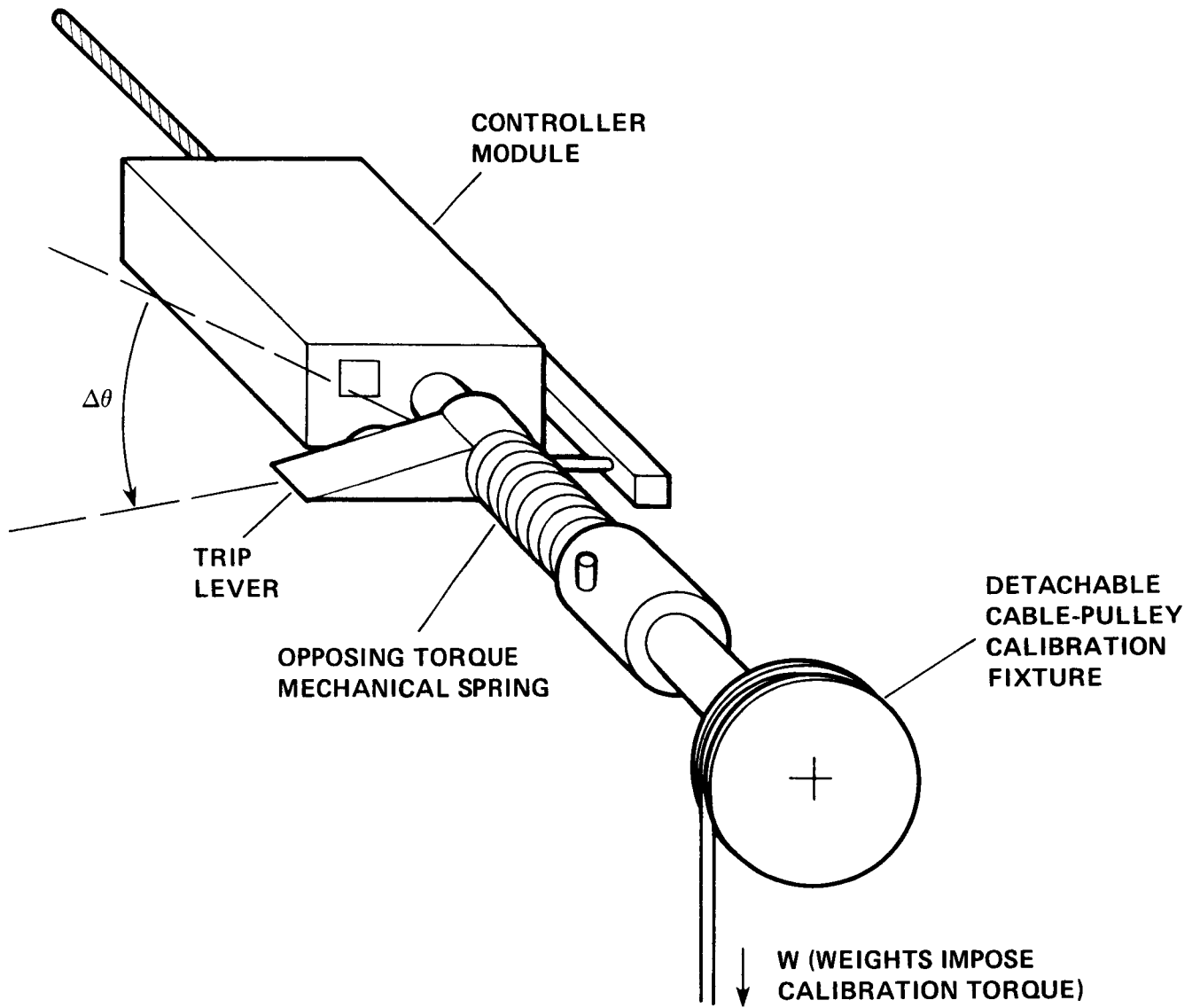
Figure 11.- Spring assembly torque calibration.
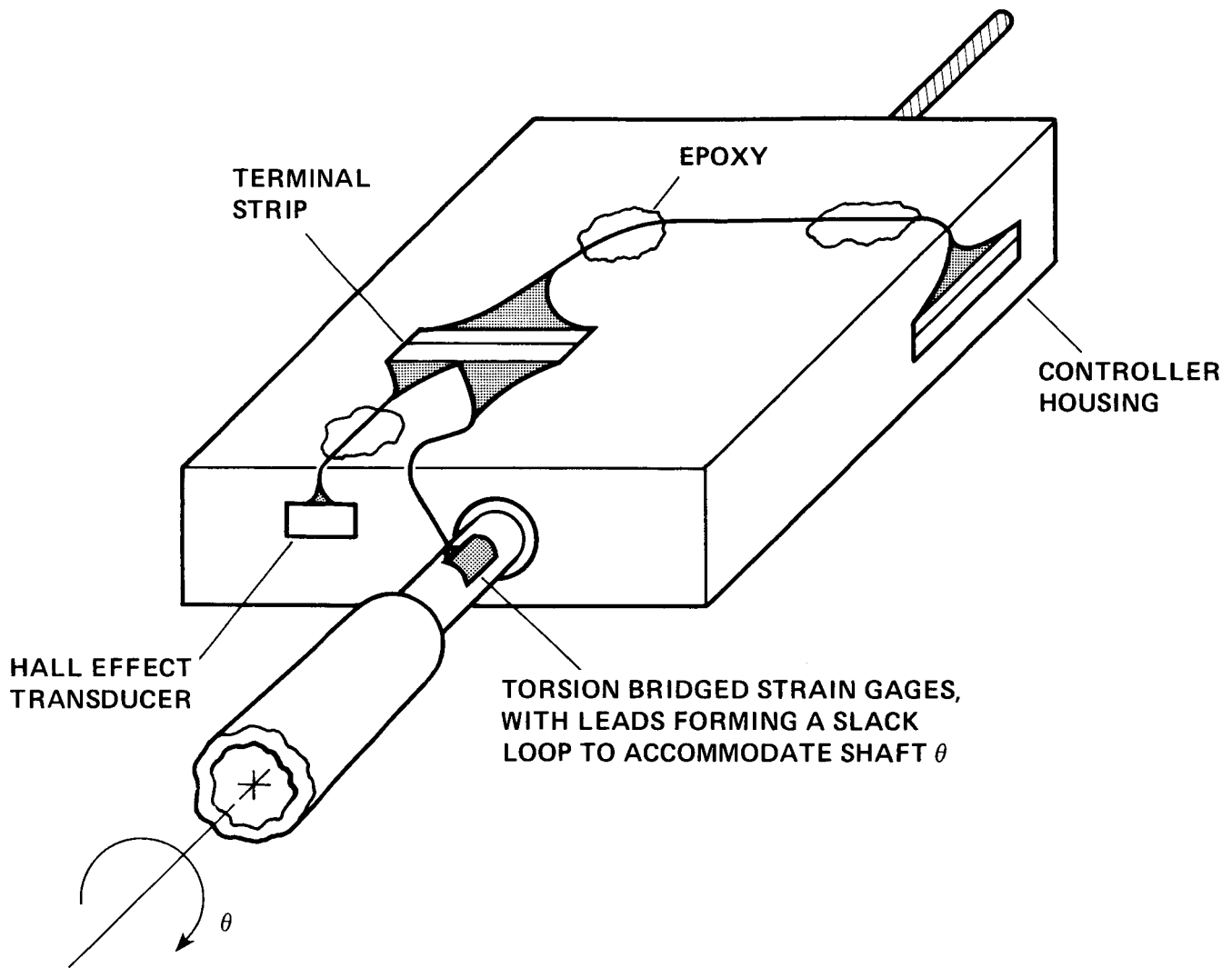
Figure 12.- Transducer placement on controller.

CF cos β sin ζ

**OUTPUT SHAFT
C.G. LOCATION**

CF sin β

CF

W sin β

W

β

ζ

Ω
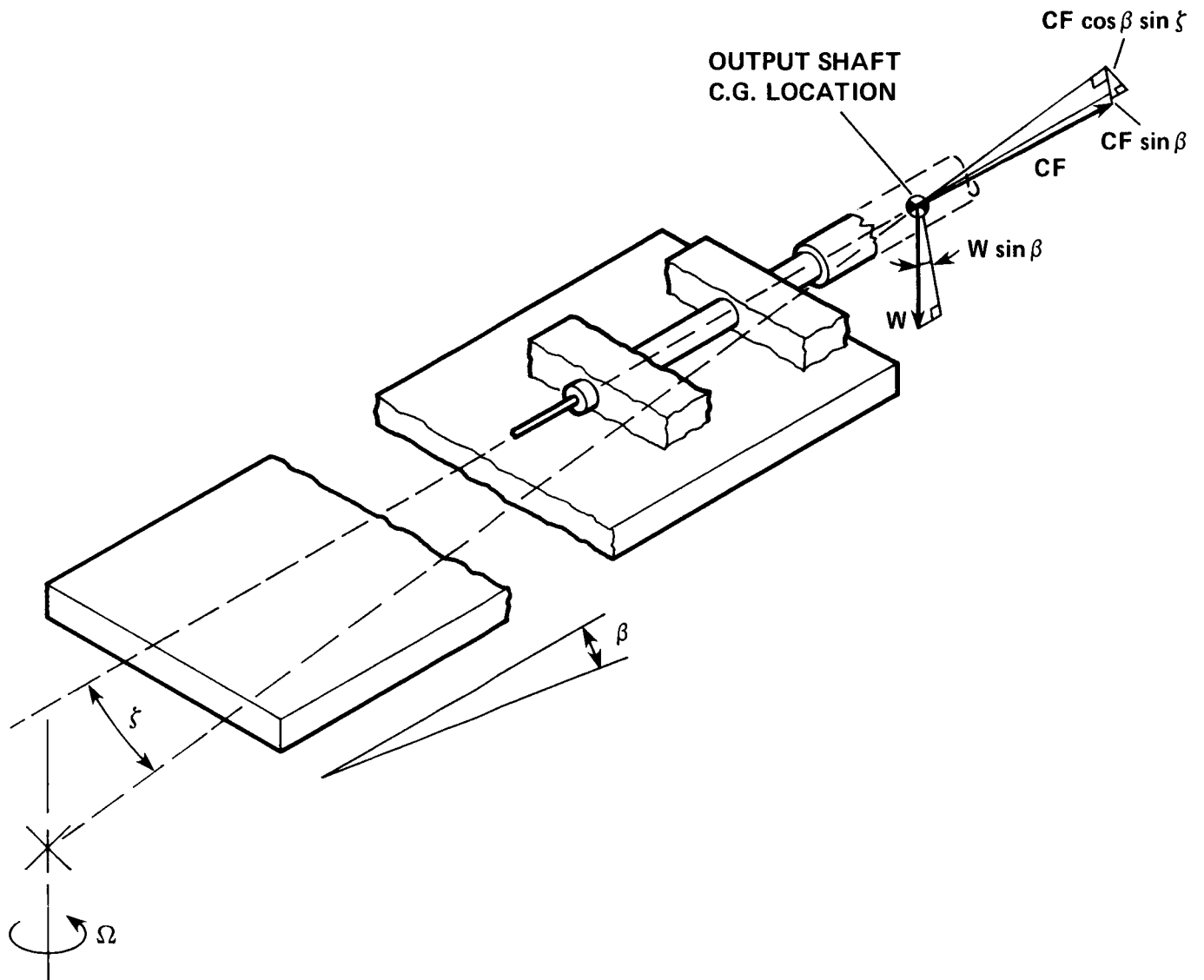
Figure 13.- Controller T_f free-body.
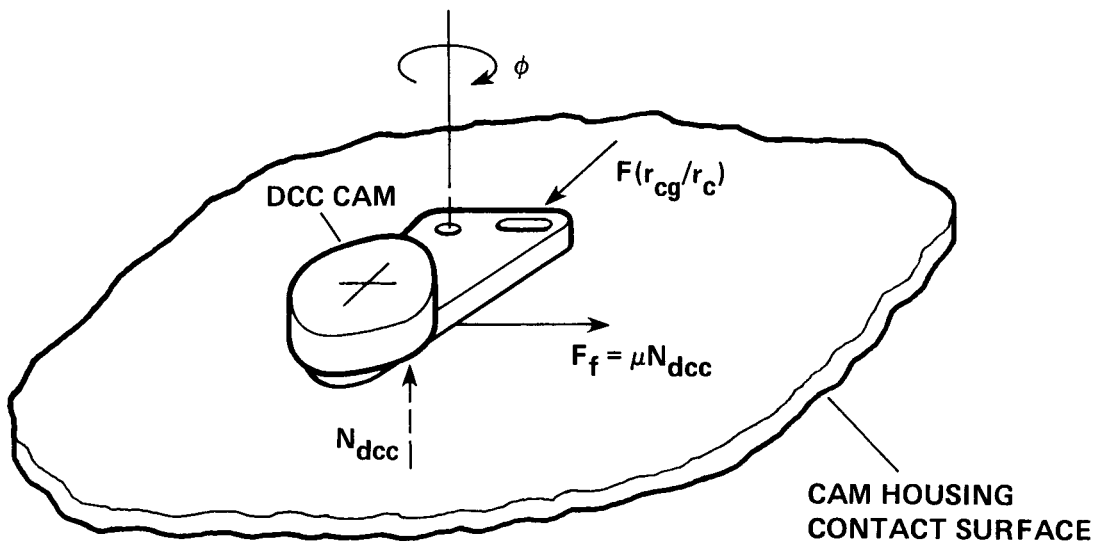
(a) DCC T_f component.

Figure 14.- Unique controller contributions to T_f.

$$F = CF_x \pm F_f$$

$$r$$

**TORQUE
OUTPUT
SHAFT**

**TRANSLATING
MASS**

$$x$$

$$F = CF_x \pm F_f$$

$$CF_x$$

$$\mu N_{mos} = F_f$$

$$N_{mos}$$
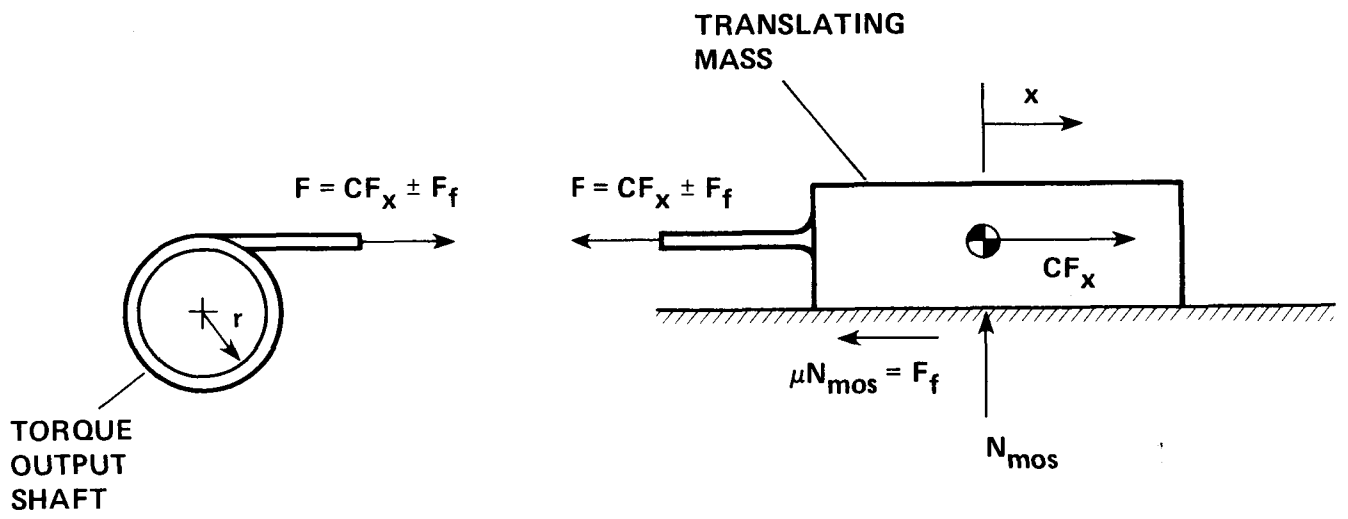
(b) MOS T_f component.

Figure 14.- Concluded.
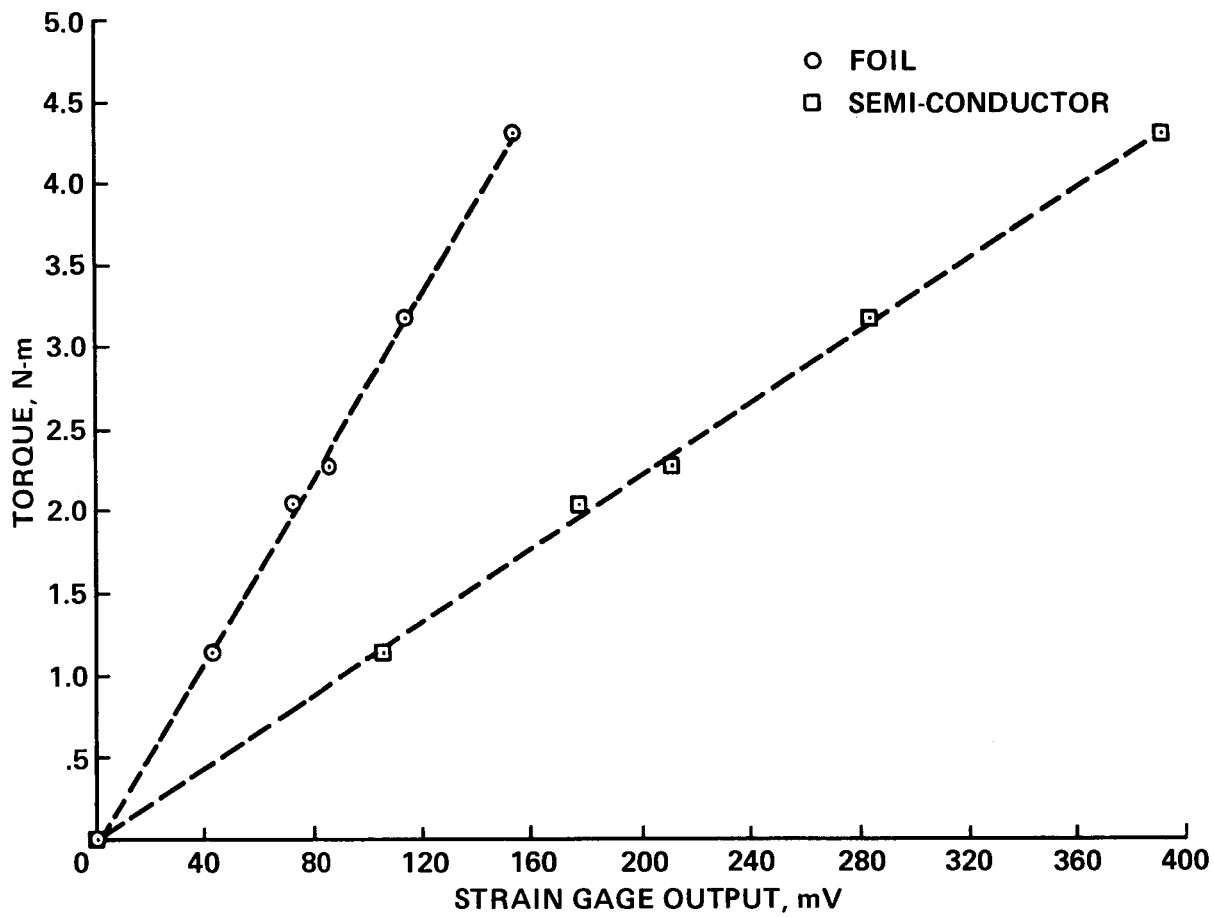
Figure 15.- Torsion-bridged strain gage calibration curve.
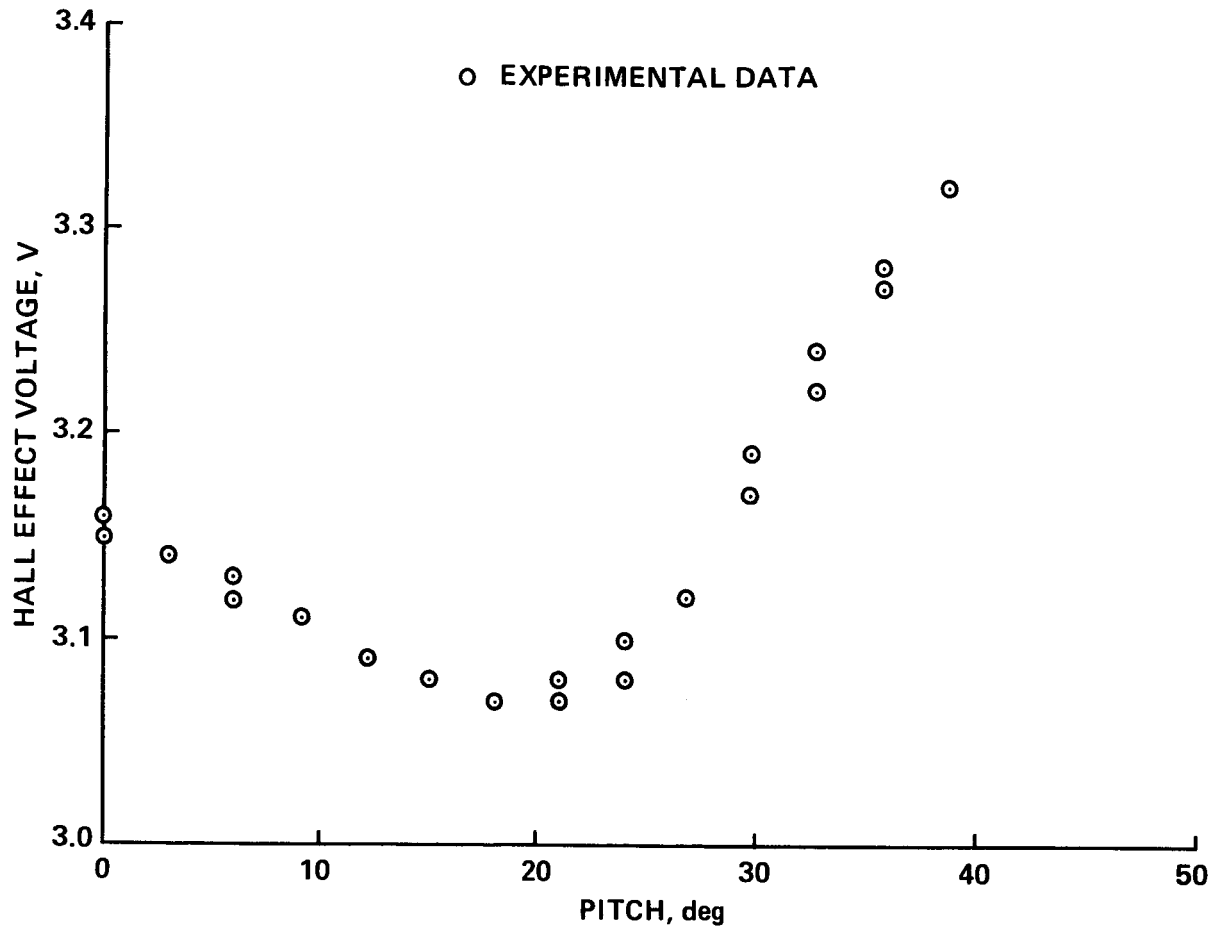
(a) Transducer calibration curve.

Figure 16.- Hall-effect torque estimate.
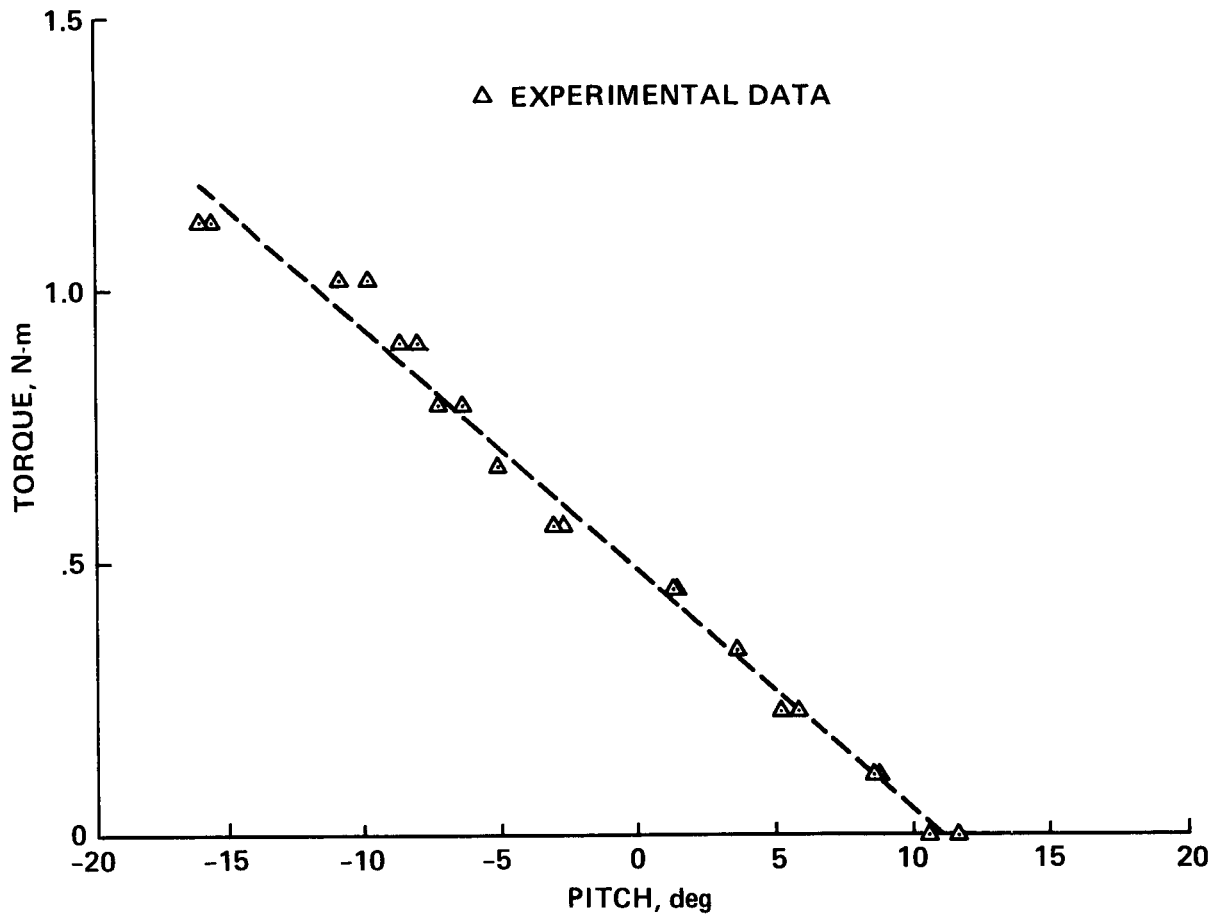
(b) Spring-constant-curve fit.

Figure 16.- Concluded.
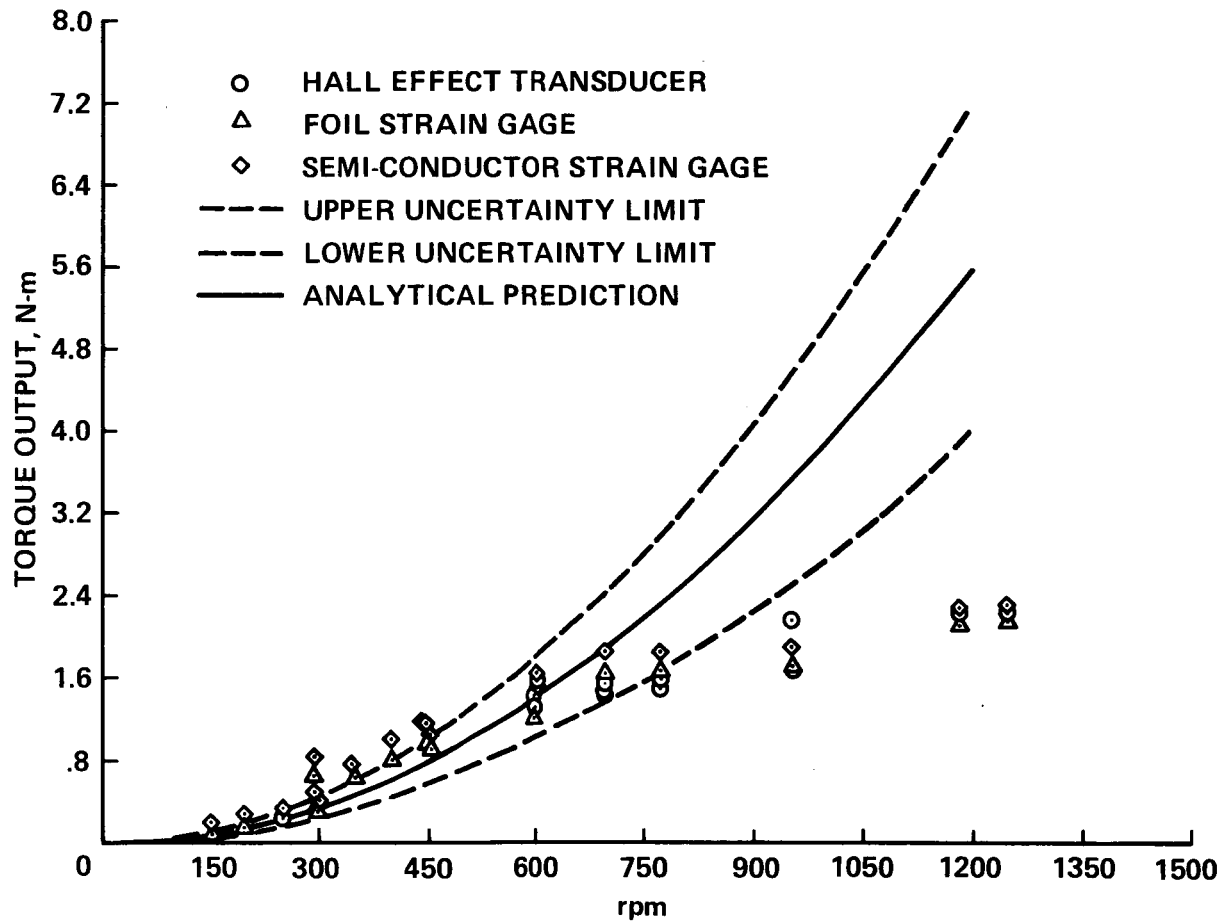
Figure 17.- Dual-cam-controller-torque output.
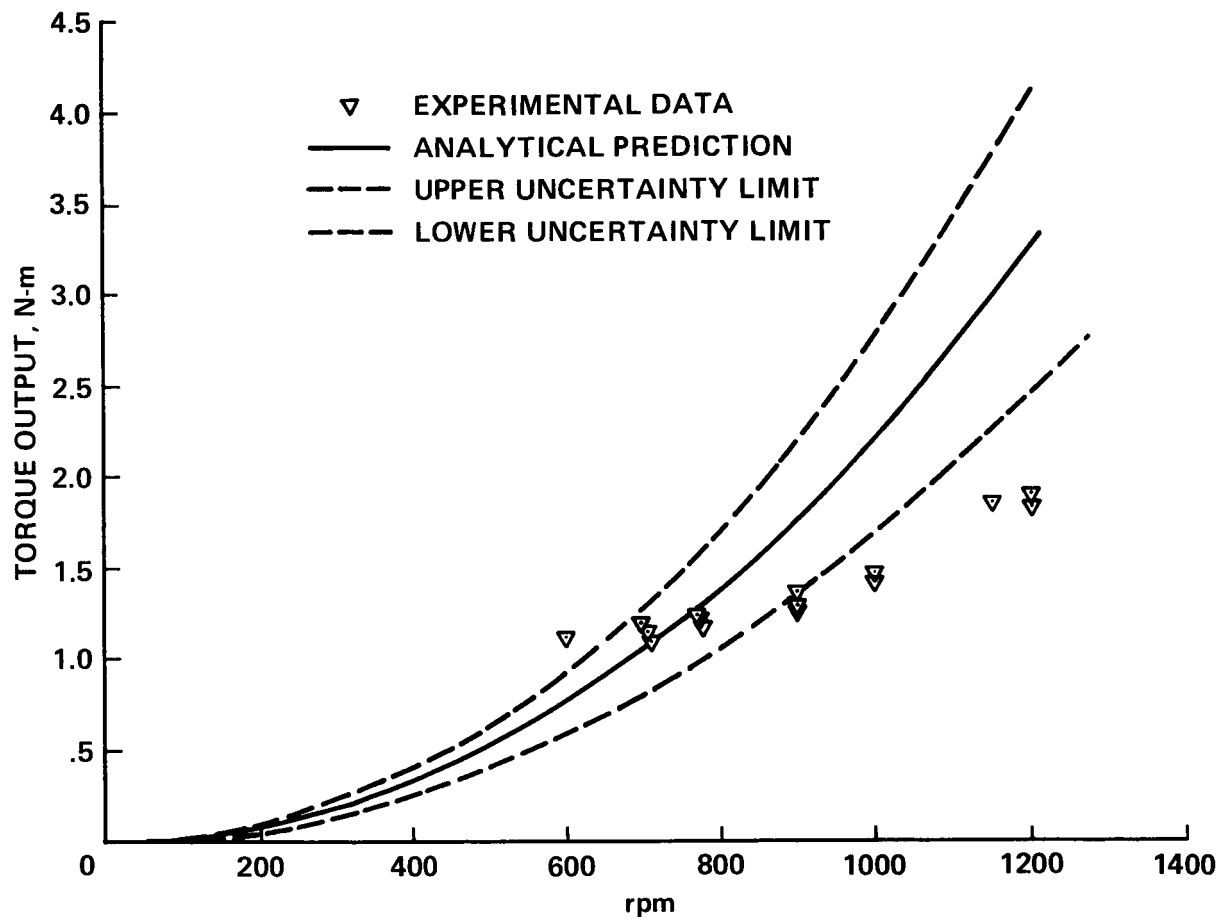
Figure 18.- Mass-on-string (pulley version) torque output.

TORSION STRAP CONTROLLER TORQUE OUTPUT AS A FUNCTION OF RPM

89° STRAP PRETWIST
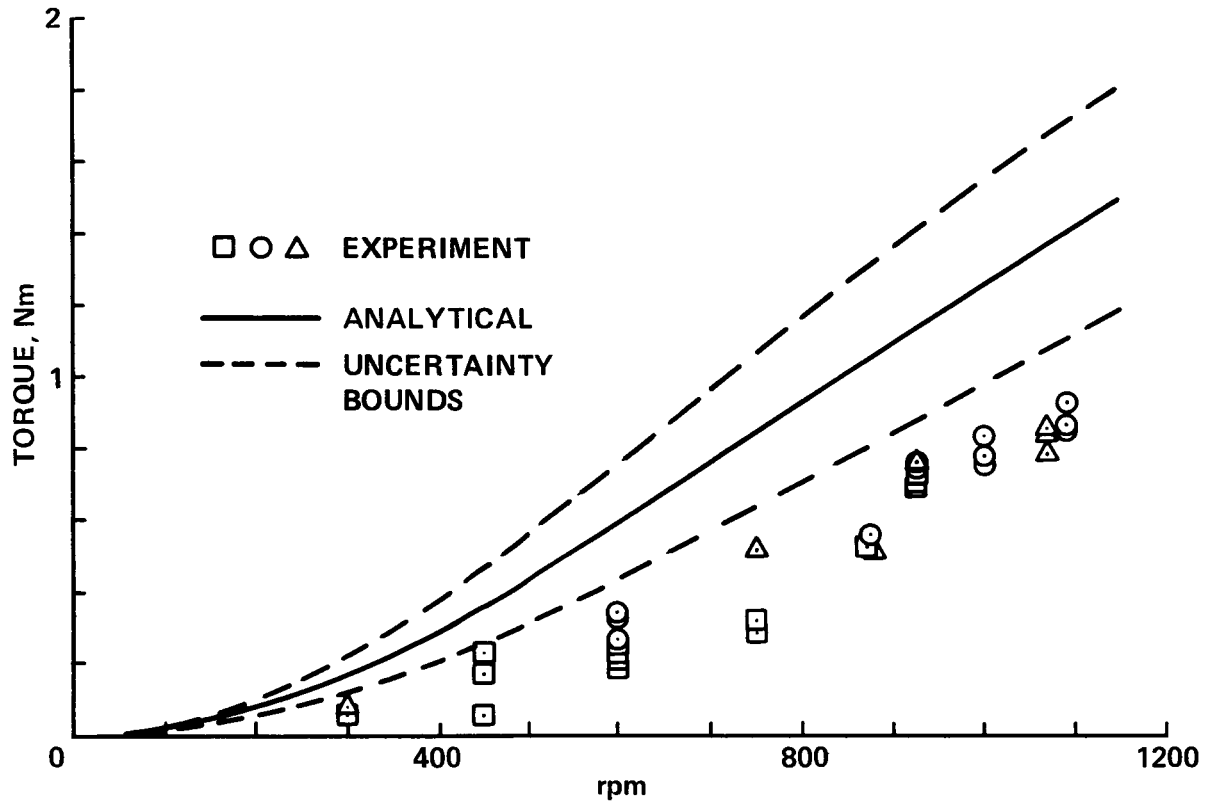
Figure 19.- Torsion-strap-controller torque output (89° strap pretwist).
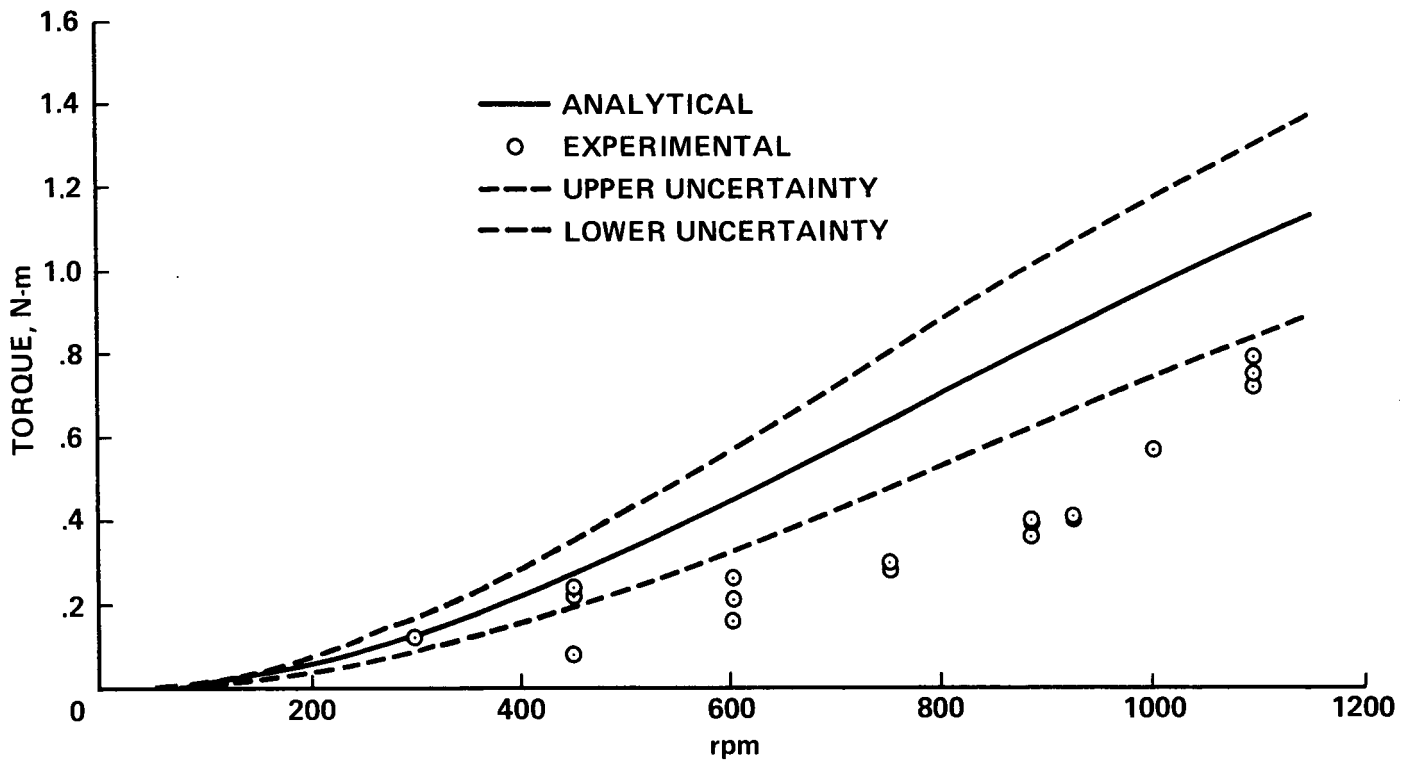
Figure 20.- Torsion-strap-controller torque output (67° strap pretwist).
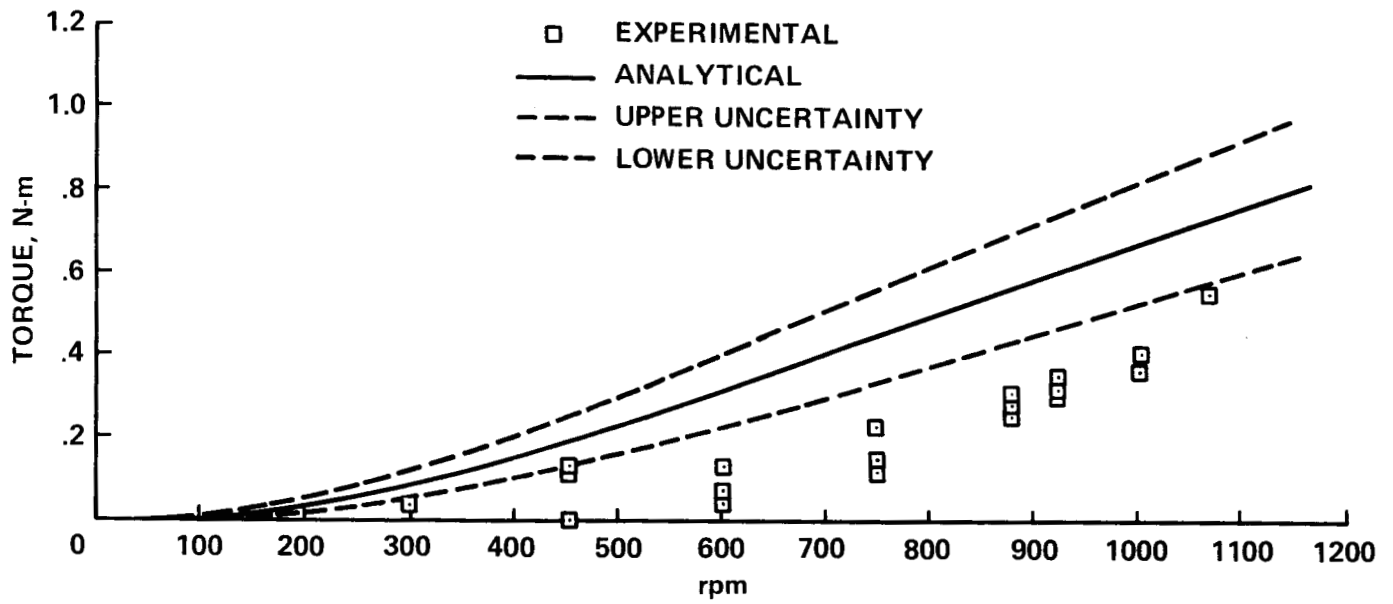
Figure 21.- TSC torque output (47° strap pretwist).
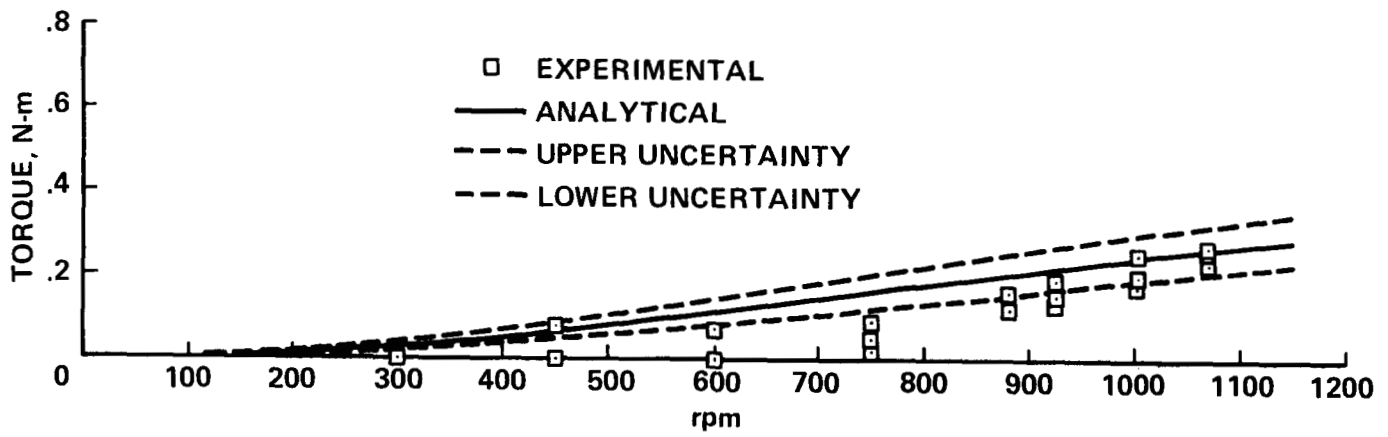
Figure 22.- TSC torque output (17° strap pretwist).
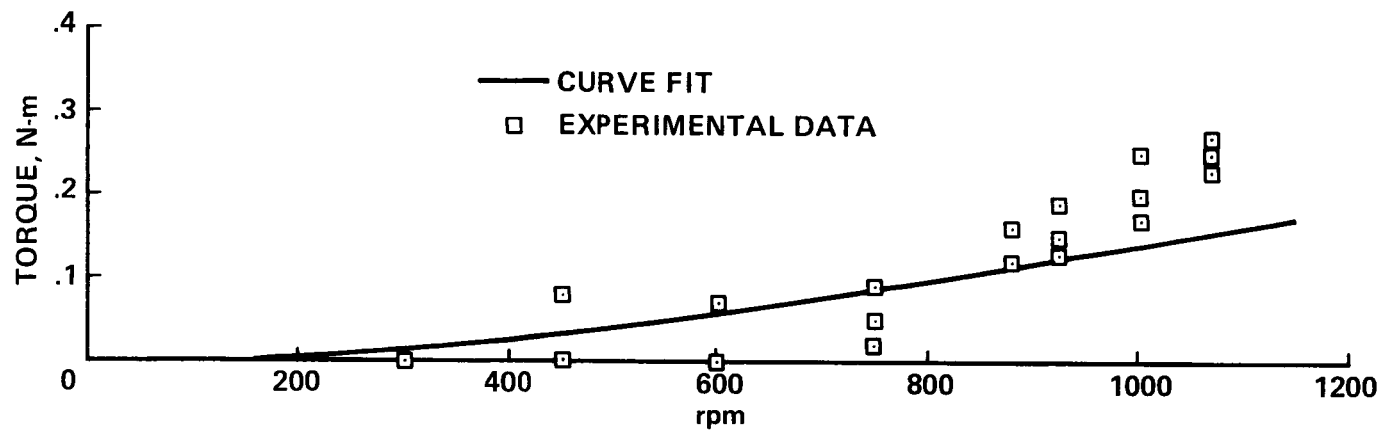
Figure 23.- TSC semiempirical model (17° pretwist).
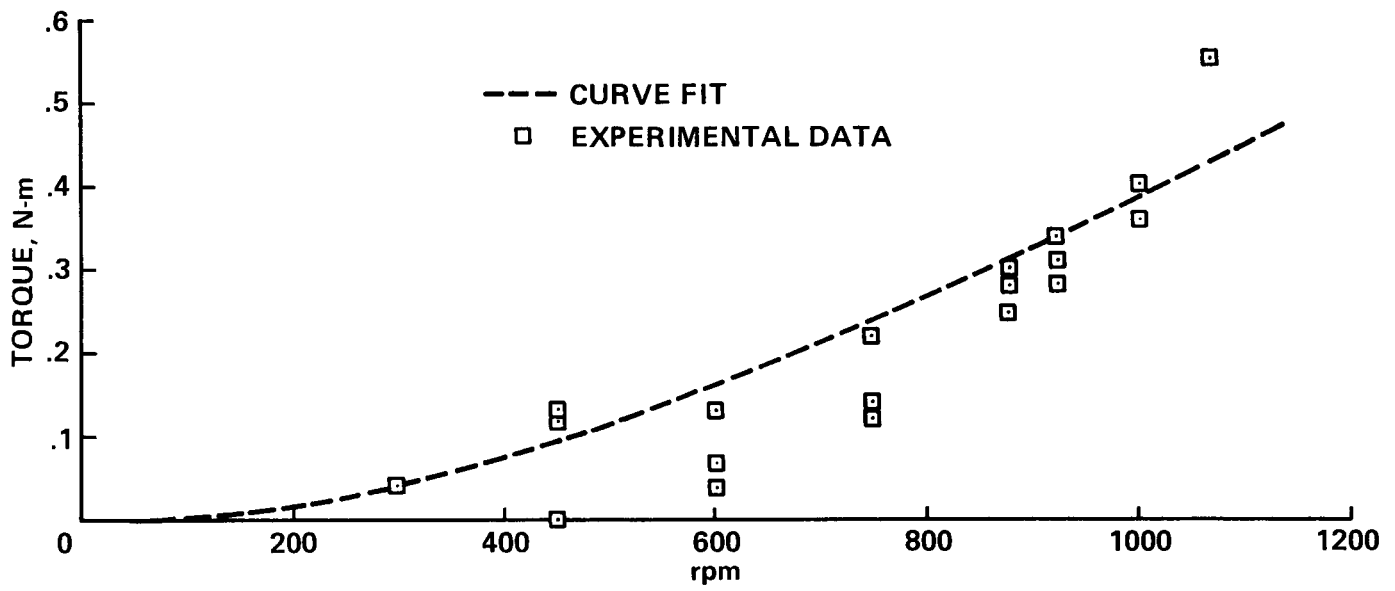
Figure 24.- TSC semiempirical model (47° pretwist).

## TORSION STRAP CONTROLLER
SEMI-EMPIRICAL MODEL
89° STRAP PRETWIST
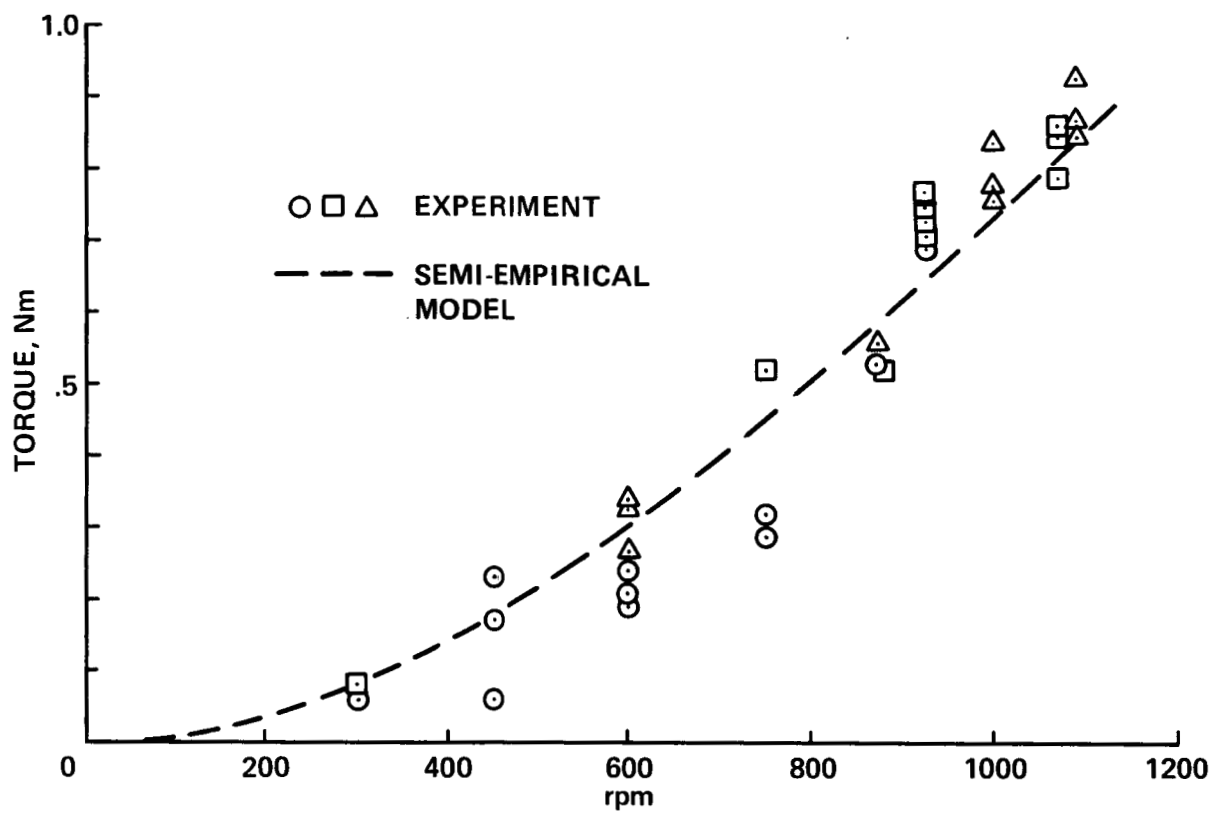
Figure 25.- TSC semiempirical model (89° pretwist).

1. Report No. NASA TM-86664	2. Government Accession No.	3. Recipient's Catalog No.
4. Title and Subtitle THE EVALUATION OF A NUMBER OF PROTOTYPES FOR THE FREE-TIP ROTOR CONSTANT-MOMENT CONTROLLER		5. Report Date February 1986
		6. Performing Organization Code
7. Author(s) Larry A. Young		8. Performing Organization Report No. A-85059
		10. Work Unit No.
9. Performing Organization Name and Address Ames Research Center Moffett Field, CA 94035		11. Contract or Grant No.
		13. Type of Report and Period Covered Technical Memorandum
12. Sponsoring Agency Name and Address National Aeronautics and Space Administration Washington, DC 20546		14. Sponsoring Agency Code 505-42-11

16. Abstract

This paper describes the development of several prototypes of a constant moment controller, a critical component of the free-tip rotor (FTR) concept. Also presented are the experimental results of a whirl test designed to select a final controller configuration to be included in a future wind-tunnel test of this innovative rotor system. A brief explanation of the FTR concept and its history are included. The paper documents the controller design constraints, each prototype's operating principle, the evaluation test, and the individual prototype test results. A recommended design is identified, along with the selection rationale.

17. Key Words (Suggested by Author(s)) Free tip, Free-tip rotor, Rotor-tip shape, Constant lift tip, Blade tip, Helicopter rotor, Constant moment controller	18. Distribution Statement Unlimited Subject category – 37		
19. Security Classif. (of this report) Unclassified	20. Security Classif. (of this page) Unclassified	21. No. of Pages 76	22. Price*